



UNIVERSITY OF AMSTERDAM

MSc Physics

-Science for Energy and Sustainability-

Master Thesis

Plasmoelectronic Measurements on Metal Hole Arrays

by

Philipp Tockhorn

Stud.nr: 10867465

July 2016

60 ECTS

September 2015 - July 2016

1st Examiner:

Prof. Dr. Albert POLMAN

Supervisors:

Dr. Jorik VAN DE GROEP

Dr. Mark KNIGHT

2nd Examiner:

Prof. Dr. Tom GREGORKIEWICZ



Abstract

Plasmon resonances are the coherent longitudinal oscillations of free carriers. The spectral response of a plasmonic metal structure which exhibits such resonances is highly dependent on geometry, interparticle interactions, dielectric environment and the optical properties of the metal itself. Classically, the optical properties of a material are fully described by its dielectric function. This entity is dependent on the density of free carriers.

In this work, we tune the plasmon resonance position of an ultrathin Au film perforated with subwavelength nanoholes by applying an electric potential to it. In order to enhance the shift of the resonance position, we employ a DEME-TFSI ionic liquid which increases the capacitance of the gold film and locally alters the refractive index of the dielectric environment. We find that upon application of a potential of 2 V, reversible redshifts of the plasmon resonance as large as 18 nm can be observed. Throughout our measurements we see a time-dependent hysteresis effect which stems from chemisorbed ions. On basis of capacitance measurements and FDTD simulations, we are able to quantitatively model the observed shifts of the plasmon resonance. We find that the largest portion is caused by a pseudocapacitance which arises from chemisorbed molecules. Moreover, we disentangle the contributions of altered charge density and local refractive index change in the ionic liquid. Based on our model, the former contributes about three quarters of the spectral shift whereas the latter contributes about one quarter.

Table of Contents

1	Introduction	3
1.1	Outline	3
2	Theory	5
2.1	Dielectric Function of Metals	5
2.2	Surface Plasmon Polaritons	7
2.3	Refractive Index Change by Concentration Change	8
3	Manipulation of the SPP resonance	9
3.1	Sample Fabrication	10
3.2	Sample Design	13
3.3	Measure Plasmonic Shifts upon Applied Voltage	16
3.4	Modelling Voltage-Induced Plasmonic Resonance Shifts	20
3.4.1	Influence of Altered Charge Density in Gold-EDL	20
3.4.2	Influence of Refractive Index Change in Ionic Liquid	22
3.4.3	Influence of Chemisorption	24
3.5	Discussion	27
3.6	Conclusions	28
3.7	Outlook	29
4	Building an Opto-Electronic Microscope	31
4.1	Software	34
4.2	Performing Measurements with the Setup	34
4.3	Characterization of the Setup	35
4.4	Data Processing	36
5	Supplementary Information	41
5.1	Dependence of SPP Resonance on Gold Thickness	41
5.2	Brendel-Bormann Model	42
5.3	Calculated Relative Changes in Charge Density and Refractive Index	42
5.3.1	Electric Double Layer Capacitance	42
5.3.2	Capacitance Due to Chemisorption	43
6	References	45

Chapter 1

Introduction

Plasmon resonances are the coherent longitudinal oscillations of free carriers. These resonances, which occur for noble metals at (near-) visible wavelengths, are strongly confined to a materials surface and have a high electric field. In order to excite such resonances, structures of subwavelength dimensions are mandatory. By adjusting the geometric properties, interparticle interactions or the local dielectric environment, the spectral response of such structures can be widely tuned.

Triggered by the advent of ever better nanofabrication and -characterization techniques, the field of plasmonics which explores this optical phenomenon has gained particular interest over the past decades. Besides the fundamental insights that were made, several applications were suggested or even came into reality. A technology which makes use of the enhanced electric field near a metal's surface to detect the vibrational states of molecules is surface enhanced Raman spectroscopy (SERS) [1]. Another approach is utilizing the high sensitivity of plasmon resonances to changes in the local dielectric environment of the metal. This can be used for unlabeled single-molecule sensing [2]. Moreover, concepts exist to incorporate plasmonic nanostructures in thin film solar cells to enhance the light trapping in thin film solar cells [3].

Recently, the possible utilization of plasmons to modify the electric properties of metal structures [4] or even to generate voltages has been explored [5].

In this work, we explore the spectral response of surface plasmon resonances to externally applied voltages. For this, a bias is applied to nanohole arrays which are in contact with an ionic liquid providing high specific capacitances. This does not only affect the density of free carriers in the plasmonic structure but also its local dielectric environment. By backing up the detected opto-electronic response with electrical measurements and FDTD simulations, quantitative understanding of the observed optical response is gained.

1.1 Outline

In chapter 2, the theoretical foundations of a metal's response to external electromagnetic fields will be investigated in terms of the dielectric function and surface plasmon polaritons. Moreover, the dependence of the refractive index on molecular polarizabilities will be described.

Throughout chapter 3, opto-electronic experiments on a plasmonic nanonhole structure will be reported: In chapter 3.1, the fabrication process of these structures is depicted and in the subsequent chapter 3.2, the basic optical response of the samples is studied, both with optical experiments and simulations. In chapter 3.3, the experimental results of shifted surface plasmon resonances will be displayed. Theoretical modelling of these shifts in chapter 3.4.1-3.4.3 is the basis to understand the observed optical behavior in chapter 3.5. In chapter 4, the realization of the opto-electronic experimental setup which was used to detect the shifts is described.

Chapter 2

Theory

In the following, key concepts which are important in the further course of this work will briefly be introduced. These include models to describe the dielectric function of metals, basic properties of surface plasmon polaritons and the description of refractive index on basis of molecular polarizabilities.

2.1 Dielectric Function of Metals

The optical behavior of a material is determined by the response of its free electrons to an impinging electric field $\mathbf{E}(t)$. The response of metals can be understood with the Drude-Sommerfeld model which assumes that electrons (with e : electron charge, m^* : effective mass, n : free electron density) are unbound and only damped by a damping constant Γ_0 [6]. The equation of motion that follows from these assumptions can be written as

$$m^* \frac{\partial^2 \mathbf{r}}{\partial t^2} + m^* \Gamma_0 \frac{\partial \mathbf{r}}{\partial t} = e \mathbf{E}(t) \quad (2.1)$$

Here, Γ_0 is the damping constant of the electron. This quantity corresponds to the inverse electron lifetime τ_0^{-1} which is dependent on a electron's lifetime for scattering processes with crystal defects (τ_{CD}), grain boundaries (τ_{GB}), phonons (τ_{e-ph}) and other electrons (τ_{e-e}) [6]:

$$\Gamma_0 = \tau_{CD}^{-1} + \tau_{GB}^{-1} + \tau_{e-ph}^{-1} + \tau_{e-e}^{-1} \quad (2.2)$$

Solving Eq. 2.1 and combining this with the definition of the polarization of metals yields an expression of the dielectric function:

$$\epsilon_D(\omega) = 1 - \frac{\omega_p^2}{\omega^2 + i\omega\Gamma_0} \quad (2.3)$$

where

$$\omega_p = \sqrt{\frac{ne^2}{\epsilon_0 m^*}} \quad (2.4)$$

The dielectric function consists of a real part ϵ_r and an imaginary part ϵ_i which describe the deflection of light and its absorption, respectively. The Drude-Sommerfeld model can

be used to describe the general trend of experimentally determined dielectric functions of metals. However, for a more accurate description of a metal's optical response, interband transitions at distinct energies have to be taken into account. A simple model to describe this behavior is the Lorentz-Drude model which adds a discrete number k of Lorentzian-type interband transitions to the Drude model [7]:

$$\epsilon_{LD}(\omega) = 1 - \frac{f_0 \omega_p^2}{\omega^2 + i\omega\Gamma_0} + \sum_j^k \frac{f_j \omega_p^2}{(\omega^2 - \omega_j^2) + i\omega\Gamma_j} \quad (2.5)$$

Here, f_0 is a weight factor for unbound electrons, f_j are weight factors of the bound electrons, ω_j are the interband transition frequencies and Γ_j are interband damping rates.

An even more accurate model for the dielectric function of metals was developed by Brendel and Bormann [8]. Their model extends the Lorentz-Drude model by superimposing the Lorentzian interband transitions with a Gaussian function. This statistical approach allows for a very good fit to measured dielectric functions. Physically, the Gaussian lineshape describes the statistic distribution of resonance frequencies.

$$\epsilon_{BB}(\omega) = 1 - \frac{f_0 \omega_p^2}{\omega(\omega - i\Gamma_0)} + \sum_{j=1}^k \chi_j(\omega) \quad (2.6)$$

where

$$\chi_j(\omega) = \frac{1}{2\pi\sigma_j} \int_{-\infty}^{+\infty} \exp\left[-\frac{(x - \omega_j)^2}{2\sigma_j^2}\right] \times \frac{f_j \omega_p^2}{(x^2 - \omega^2) + i\omega\Gamma_j} dx \quad (2.7)$$

Here, σ_j describe the damping of the Gaussian oscillators.

Fig. 2.1a and b shows the real and imaginary part of the gold dielectric function for the three different models introduced above. The Drude model proves to be accurate for the low energy part of the dielectric functions ($E < 2.1$ eV). In the regime of higher energies where interband transitions occur it fails to describe the measured data. In contrast to this, the Lorentz-Drude and the Brendel-Bormann model are able to reproduce the trends well. For the real part ϵ_r , only minute deviations between the two models occur, whereas for the imaginary part ϵ_i , the Brendel-Bormann model performs better.

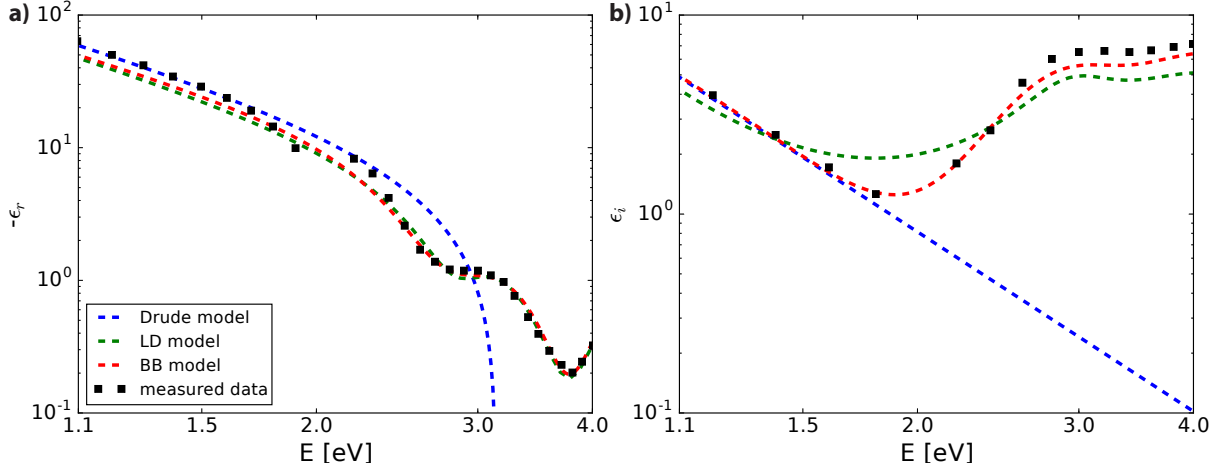


Fig. 2.1: a) Real and b) imaginary part of the dielectric function of gold. The black squares are measured data by Thèye [9]. The dashed blue line represents the Drude model which was fitted to the low-energy part ($E < 2.1$ eV). The dashed green and red lines display the Lorentz-Drude (LD) and Brendel-Bormann (BB) model, respectively. Note that the parameters for LD and BB model were taken from [7] and that the y-scale for a) and b) are different. The deviation from measured data in the low-energy regime (< 2.1 eV) is due to a fit experimental data in the infrared which are not shown here.

2.2 Surface Plasmon Polaritons

Surface plasmon polaritons (SPP) are the propagating surface modes at a metal/dielectric interface and are comprised of the oscillating surface electrons of the metal and its associated electromagnetic field [10]. In the case of a single interface, the dispersion relation which determines the modes that can be excited by an impinging electromagnetic wave of frequency ω can be solved analytically on basis of the conservation of parallel wave vector momentum $k_{||}$.

$$k_{||}^2 + k_{z,d/m}^2 = \epsilon_{d/m} \cdot \left(\frac{\omega}{c}\right)^2 \quad (2.8)$$

Here, the indices d/m represent dielectric and metal, respectively and $\frac{\omega}{c}$ denotes the momentum of free space photons. Solving this equation for $k_{||}/k_{SPP}$ yields the dispersion relation of surface plasmons for a single interface [11]:

$$k_{SPP} = \frac{\omega}{c} \sqrt{\frac{\epsilon_d \epsilon_m}{\epsilon_d + \epsilon_m}} \quad (2.9)$$

If more complex structures are investigated, the dispersion relation has to be calculated from the parallel wave vector conservation at every interface in the structure.

For common material constants of dielectrics and metals, k_{SPP} is usually larger than the free space wave vector of photons [12]. This means that free space photons cannot directly couple to SPPs but have to gain an additional wave vector momentum. One way to gain this missing momentum is to periodically perforate the metal film with holes [10, 13]. At these holes, which are separated by Λ , light can be diffracted (with diffraction orders $m = 1, 2, \dots$) and thereby gain additional momentum to the in-plane momentum $k_{||}$ so that

$$k_{SPP} = k_{||} \pm m \frac{2\pi}{\Lambda} \quad (2.10)$$

2.3 Refractive Index Change by Concentration Change

The optical response of a dielectric medium consisting of a number of molecules can be described with the molecular polarizability α and the number density n using the Lorentz-Lorenz equation [14]. This equation combines the dielectric function with the polarizability of molecules. If a medium consist of different kinds of molecules, this equation still holds but can be written as a sum of the individual contributions (in CGS units):

$$\frac{n^2 - 1}{n^2 + 2} = \sum_i \frac{4}{3} \pi n_i \alpha_i \quad (2.11)$$

The polarizability of a molecule can be interpreted (in CGS units) as the interaction volume of that molecule with light. Typically, this volume has dimensions of some \AA^3 .

The molecular polarizability can be well estimated by adding hybridized atomic polarizabilities of bond atoms rather than those of atoms [15]. These values are determined from measurements on homologous molecules.

Chapter 3

Manipulation of the SPP resonance

From Eq. 2.9 it can be seen that the free space frequency at which photons can couple to SPPs is dependent on the dielectric function of both the metal and the surrounding dielectric media. In the case of the metal, the dielectric function greatly depends on the free electron density parameter which is mostly determined by the type of metal. Another effect on the dielectric function of nanoscale metallic structure can be its size and shape. It has been found that the associated spatial confinement mainly alters a metal's dielectric function by changing the interband transitions [16].

An *in situ* change of a metal's dielectric function can be reached by manipulating the free electron density by means of externally applied electric potentials. A common way to increase the relative change in charge density is to enhance the capacitance of the investigated plasmonic structure.

Following this strategy, shifts in resonance wavelength were demonstrated for different nanoparticle geometries such as nanospheres [17,18], -rods [19,20], -disks [21] or -holes [21] supporting localized surface plasmon resonances (LSPR). For instance, silver nanoparticles were shown to exhibit a reversible shift of the LSPR as large as 20 nm [18] for a change in applied potential of 2 V. A common observation throughout different studies is that a blue-shift of the resonance is accompanied by a narrowing and amplitude increase of the resonance peak and a red-shift is accompanied by a broadening in energy and a decrease in amplitude [17–20].

The second parameter that can change the plasmon resonance wavelength *in situ* is the refractive index of the surrounding dielectric medium. As the plasmon resonance position is approximately linearly dependent on a change of the refractive index [22], this effect is used to detect the adsorption of single molecules to plasmonic nanoparticles [2] or to measure small concentrations of heavy metal ions with high accuracy [23].

The preceding considerations regarding the tunability of plasmon resonances suggest that when enhancing the capacitance with ionic liquids, both the influence of the altered charge density and the influence of the altered refractive index near the surface have to be taken into account. The interplay of these two contributions will be investigated in the following. To this end, an experimental structure comprising of a thin gold film which is periodically perforated with subwavelength holes is fabricated and characterized. This kind of structure supports SPPs whose resonance position can easily be tailored by tuning the geometric di-

mensions [12]. To enhance the plasmonic structure's capacitance, it will be combined with a water-based ionic liquid carrying organic ions.

3.1 Sample Fabrication

The plasmonic structure comprises of an ultrathin gold film on top of a dielectric Al_2O_3 -layer and silver. The gold film which is perforated with holes separated by 290 nm supports a surface plasmon polariton (SPP). This is the main optical property that will be investigated in the following. The main optical benefit of this structure is that it can support unity absorption as the gold and silver layer together constitute a Fabry-Pérot resonator which, together with the high reflectivity of silver, can be tuned to critical coupling of the plasmon resonance in the gold film [24] (see chapter 3.2). Moreover, the layer structure displays a platform for electrical measurements as a bias can be applied between the gold and silver film. Essentially, the two metal layers constitute a parallel plate capacitor which slightly enhances the possible relative change in charge density.

In the following, we describe the fabrication of this nanostructured device. Electric isolation between gold and silver layer is achieved by placing the hole arrays on $150\text{ }\mu\text{m} \times 150\text{ }\mu\text{m}$ large pads and electrical contacting is facilitated with thick gold pads next to every hole array (see Fig. 3.1a).

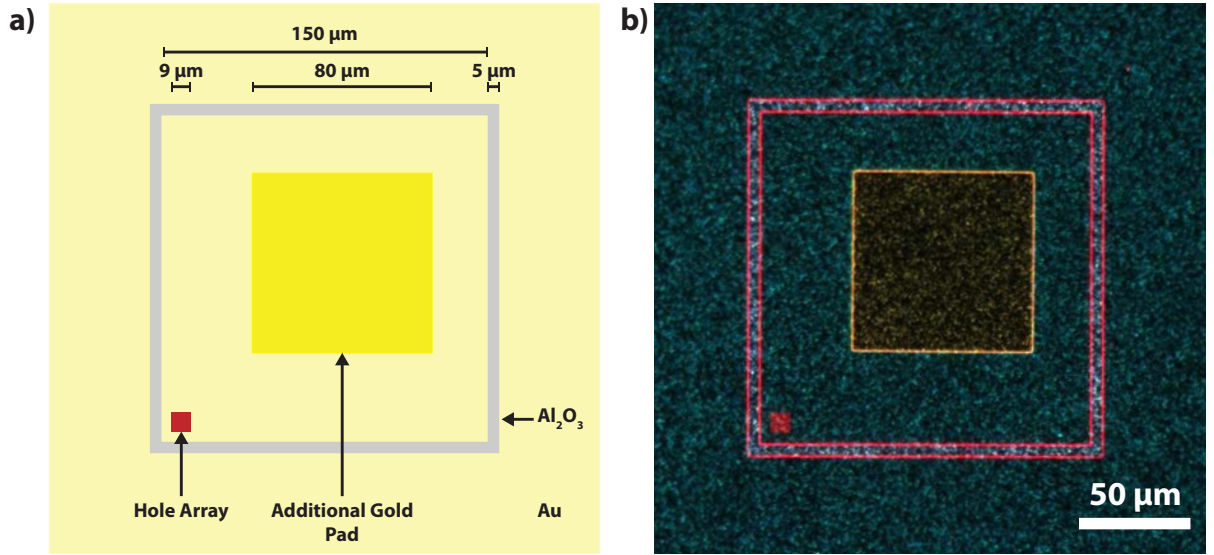


Fig. 3.1: a) Sample Geometry with dimensions of contact pad ($150 \times 150\text{ }\mu\text{m}$), hole array ($9 \times 9\text{ }\mu\text{m}$) and additional gold pads ($80 \times 80\text{ }\mu\text{m}$) b) darkfield micrograph image of the fabricated structure.

As sample substrates, $12 \times 12 \times 1\text{ mm}$ glass panes are used (Fig. 3.2a), which are cleaned using a base piranha recipe. Onto these substrates, a 15 nm chromium adhesion layer (rate: 0.15 nm/s, 150 mA sputter current) and a 330 nm silver back reflection layer (rate: 1 nm/s, 150 mA sputter current) are sputter coated (Fig. 3.2b). A homogeneous intermediate layer of

Al_2O_3 with large resistivity is deposited onto the sample by means of atomic layer deposition (1580 cycles, 150°C) using the precursors trimethylaluminum (TMA) and H_2O (Fig. 3.2c). In the next step, a three layer structure of PMMA, germanium and HSQ electron resist is deposited on the sample (Fig. 3.2d). The merit of this structure is that the nanoscale structures can be written with high resolution in the HSQ resist and the PMMA facilitates lift-off after the deposition of gold. After prebaking the sample at 150°C for 3 min, a 230 nm thick PMMA-layer (1500 rot/s, acceleration 1500 rot/s, 45 s) is spin-coated and postbaked for 3 min at 150°C . Next, a 25 nm germanium layer is thermally evaporated (rate: 0.5 \AA/s) and finally a 70 nm layer of negative electron resist is spin-coated (HSQ-Fox 15: Methyl Isobutyl Ketone (MIBK) (1:2), 3000 rot/s, acceleration 1500 rot/s, 45 s) onto the sample and baked out for 2 min at 180°C .

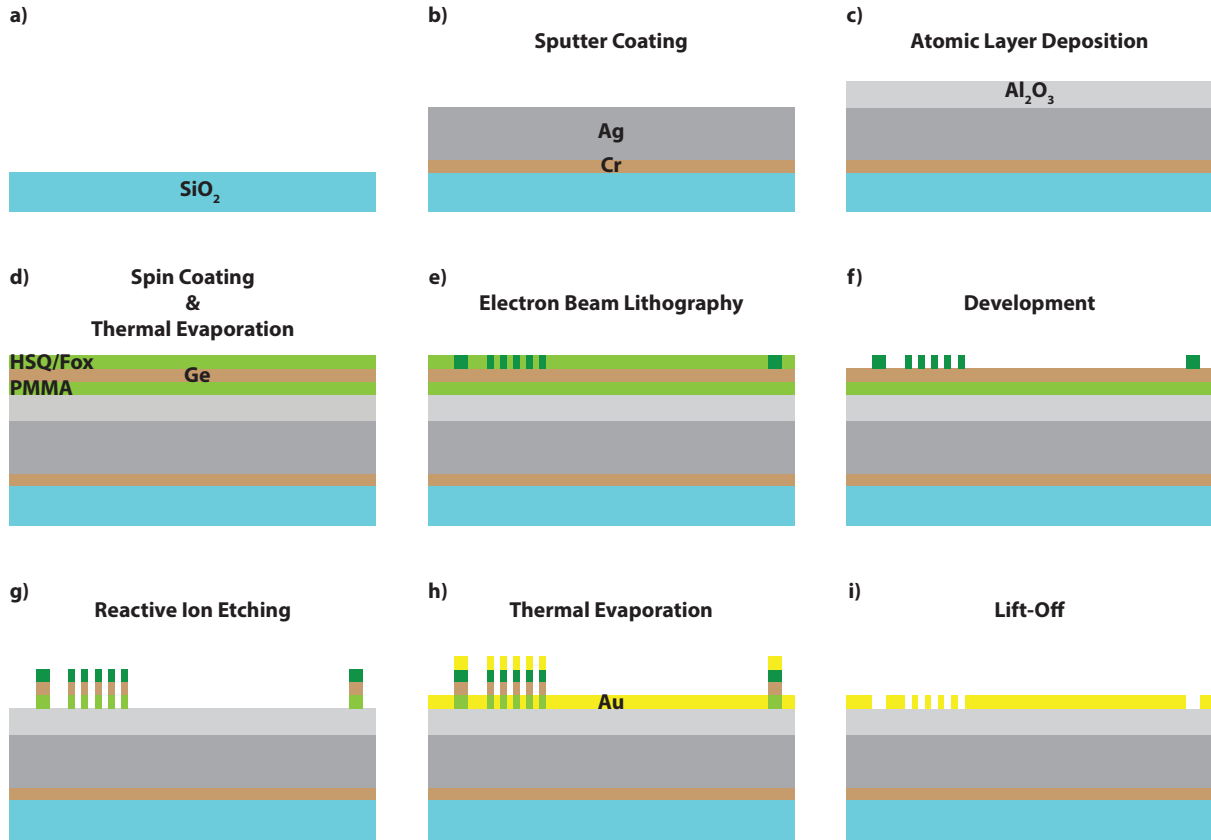


Fig. 3.2: a-i) Schematic cross sections of the fabrication process for hole arrays. The respective dimensions do not correspond to the real dimensions.

Subsequently, electron beam lithography (EBL) is employed to define the hole array structure with a pitch of 290 nm at doses ranging from $200\text{--}400 \mu\text{C}/\text{cm}^2$ (proximity correction, $10 \mu\text{m}$ aperture, 20 kV) in the HSQ resist (Fig. 3.2e). The contact pads with dimensions of $150 \times 150 \mu\text{m}$ and a width of $5 \mu\text{m}$ are written at a dose of $300 \mu\text{C}/\text{cm}^2$ ($30 \mu\text{m}$ aperture, 20 kV) into the resist. After the EBL step, the HSQ resist is developed for 1 min in MF-319 developer at 50°C and rinsed in deionized water (Fig. 3.2f). Next, reactive ion etching (Fig. 3.2g) is used to transfer the pattern through the sacrificial Ge layer (12.5 sccm SF_6 , 2.5 sccm O_2 , 3 min, backpressure 8 mtor, strike pressure 20 mtor) into the PMMA layer (25 sccm O_2 ,

4:30 min, backpressure 5 mtor, strike pressure 30 mtor). The PMMA is underetched which facilitates the subsequent lift-off. Thermal evaporation is employed to deposit a 20 nm thin gold film (rate 0.5 Å/s) onto the sample (Fig. 3.2h). Finally, the redundant gold and resist is removed with 10 min of megasonication in acetone which is interrupted in order to blow gold flakes off the surface with a syringe (Fig. 3.2i). Finally, the samples are ultrasonicated in iso-propanol (IPA) for 1 min.

In order to be able to relate exposure doses to actual hole diameters, the dimensions of holes at different doses is measured with an SEM. For every dose factor, the average diameter is calculated from ten horizontally and ten vertically measured holes. As can be seen from Fig. 3.3a and b, the hole diameter is significantly varying for doses of 200 and 400 $\mu\text{C}/\text{cm}^2$, respectively. The results of SEM image analysis are displayed in Fig. 3.3c, which connects the doses to corresponding diameters ranging from 97 to 145 nm.

In general, holes with larger diameters tend to be more circular than those with smaller doses, indicating that the lift-off works better.

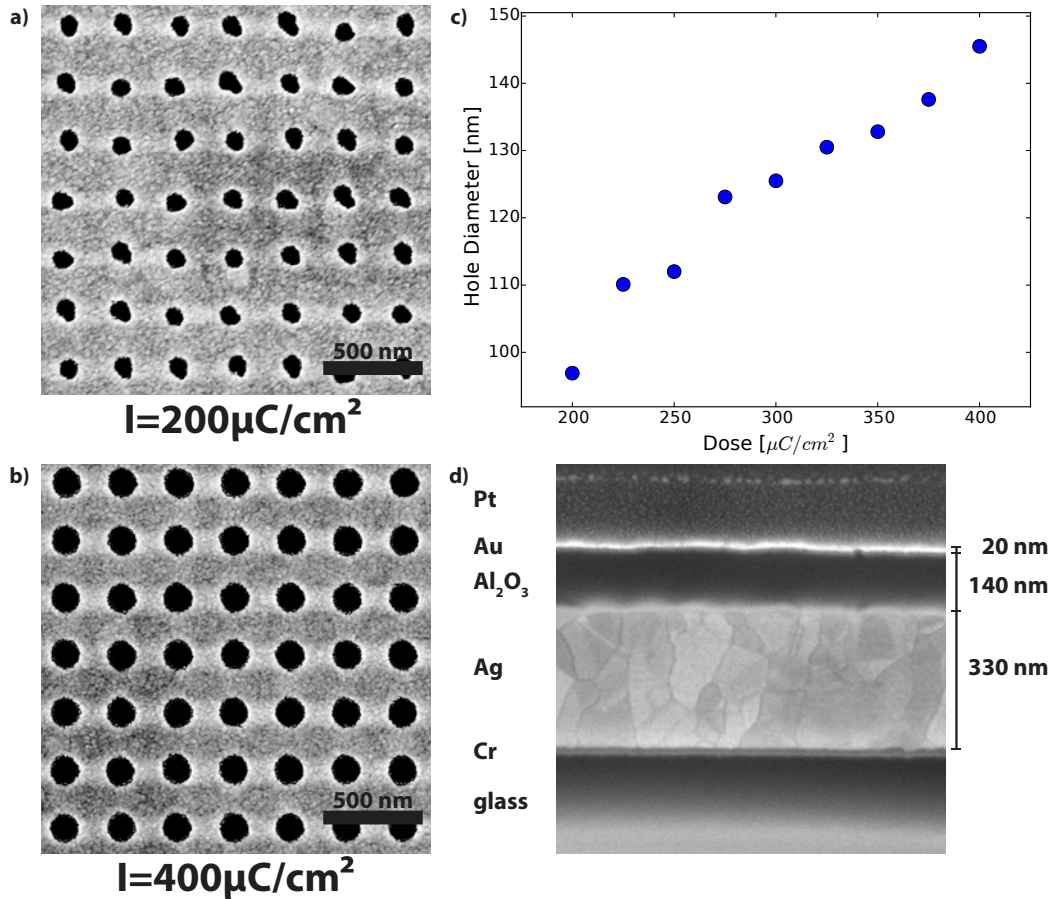


Fig. 3.3: a), b) 5 kV SEM images of hole arrays for exposure doses of 200 and 400 $\mu\text{C}/\text{cm}^2$, respectively c) measured hole diameters vs. exposure dose d) 260 kx, 5 kV SEM cross section of the fabricated structure. Note that the Platinum (Pt) layer was deposited for better imaging.

In a second fabrication step, thicker pads of gold are deposited onto the devices. These pads facilitate the contacting of the 20 nm thin gold film as they avoid a short caused by puncturing. For this, an adhesion layer of bis(trimethylsilyl)amine (HMDS) is spin-coated (4000 rot/s, acceleration 1000 rot/s, 35 s) underneath a 420 nm thick layer of positive ZEP resist (ZEP 520a, 1200 rot/s, acceleration 700 rot/s, 40 s, Fig. 3.4a) and E-Spacer (2000 rot/s, acceleration 400 rot/s, 45 s). Subsequently, 80 x 80 μm big squares are written with EBL onto each pad (dose: 100 $\mu\text{C}/\text{cm}^2$, 30 μm aperture, Fig. 3.4b). Afterwards, the E-spacer is removed by rinsing the sample twice in H_2O (30 and 15 s, different beakers). The ZEP resist is developed by rinsing the sample 60 s in pentyl acetate, 15 s in MIBK:IPA (9:1) and 15 s in IPA (Fig. 3.4c). Then, a 100 nm thick gold film is thermally evaporated (2 $\text{\AA}/\text{s}$, Fig. 3.4d). Finally, the redundant gold and resist is removed from the sample by megasonication (10 min) in acetone and ultrasonication (1 min) in IPA (Fig. 3.4e). As before, a syringe is used to blow gold flakes off the surface. A darkfield micrograph of the as-fabricated sample is displayed in Fig. 3.1b.

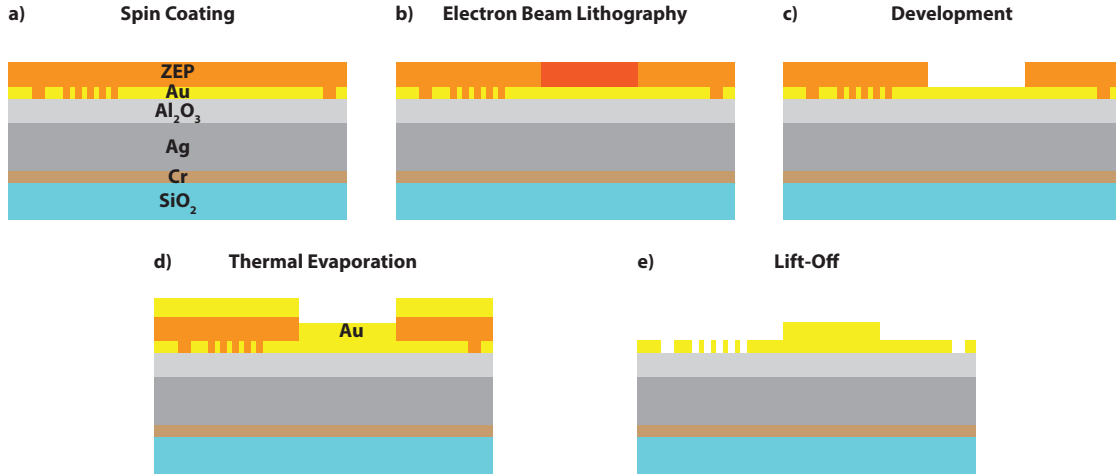


Fig. 3.4: a-e) Schematic cross sections of the fabrication process for additional gold pads. The respective dimensions do not correspond to the real dimensions.

3.2 Sample Design

We use finite-difference time-domain (FDTD) simulations to study the optical properties of the plasmonic structures which are described in chapter 3.1. For this, periodic hole arrays with the corresponding dimensions are built in Lumerical [25]. Fig. 3.5 shows the cross section of a unit cell in the simulation. The dielectric functions of silver and gold are described with a Brendel-Bormann model according to the parameters found by Rakic et al. [7] and the dielectric function of Al_2O_3 is represented with values determined from Variable Angle Spectroscopic Ellipsometry (VASE). In order to model the effect of a water based-electrolyte, the index of the surrounding medium is set to 1.31. Based on an Al_2O_3 thickness of 140 nm (Fig. 3.3d), the optical response of structures with diameters ranging from 90 to 150 nm, a pitch of 290 nm and a gold layer with a thickness of 20 nm are simulated. A plane wave in the wavelength range 500-1100 nm is injected 180 nm above the

structure and monitors 50 nm below and 230 nm above the gold film record transmission and reflection. The top and bottom boundary conditions are set to PML and metal, respectively. For improved computation time, the side boundaries parallel to the plane wave source are set to anti-symmetric and those perpendicular are set to symmetric (not displayed in Fig. 3.5). In order to better resolve the optical response of the thin gold film, an additional mesh with 1 nm spacing in either direction is overriding the background mesh (5 nm spacing in either direction). This fine mesh covers the z-interval between 10 nm above and below the 20 nm thick gold film (see Fig. 3.5).

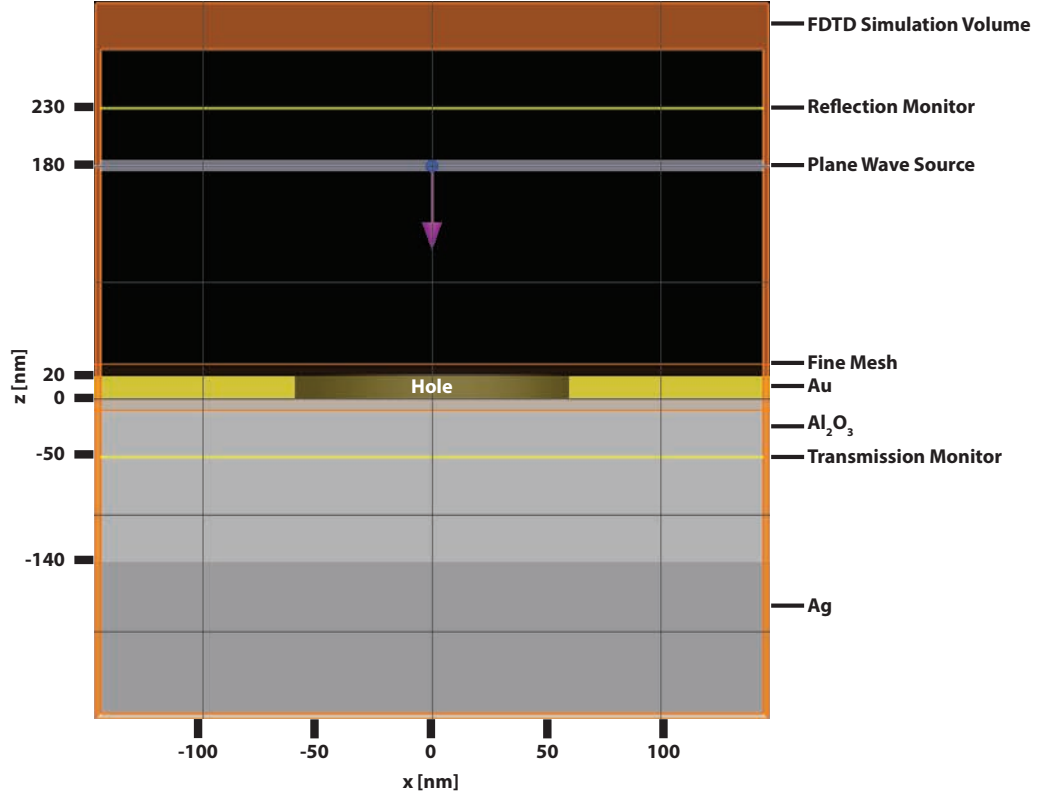


Fig. 3.5: Cross section of a unit cell in the Lumerical FDTD environment. For visual clarity, the symmetric and antisymmetric setting was deactivated.

Additionally, the absorption spectra for hole arrays with different diameters are measured with an microscopy setup for reflection measurements (see chapter 4). As the silver layer is blocking the downpath, the absorption can simply be calculated from the reflection signal: $A = 1 - R$.

Fig. 3.6a and b show the simulated and measured absorption spectra for the above described structure for different hole diameters. The main feature of interest for both, simulated and measured spectra is the SPP peak around 800 nm. Remarkably, the absorption amplitude surpasses 80 % for most of the simulated and all measured spectra. The low thickness of the gold film (≈ 20 nm) supports a coupling of SPPs at its front and back side which strongly enhances the absorption of light [26]. Moreover, an increase in hole diameter leads to a redshift and broadening of the resonance due to enhanced coupling of dipole oscillations to propagating SPPs [27]. For the simulated spectra, the SPP peak position redshifts by about

50 nm for diameters increasing from 90 (dark purple line) to 150 nm (green line). In contrast to this, the measured spectra show a redshift of 76 nm when increasing the hole diameter from 97 (dark purple line) to 145 nm (green line). The mismatch between simulated and measured spectra in resonance position and height can mainly be attributed to deviations of the dielectric functions calculated with the Brendel-Bormann model. In particular, the parameters used for the Brendel-Bormann model were determined with measurements on bulk metals whereas thin films might exhibit different behavior. Another major influence on the SPP resonance is displayed by the thickness of the approximately 20 nm thin gold layer: A deviation of only two nanometer in thickness causes already a shift of about 15 nm for a specific geometric configuration (see Fig. S1a). Thickness deviations of this magnitude can be explained with the limited accuracy of the used thermal evaporation setup. Further factors adding to the discrepancy between measurement and simulation might be the surface roughness of the gold film and not perfectly circular holes in the fabricated samples (see Fig. 3.3).

The smaller peak width in the experiment in comparison to the FDTD simulations can mainly be explained with the restrictions imposed by the numerical aperture (NA) of the objective used for the measurements. An NA of 0.40 corresponds to a maximum collection angle of 23.6° while in the simulations all scattered angles are collected.

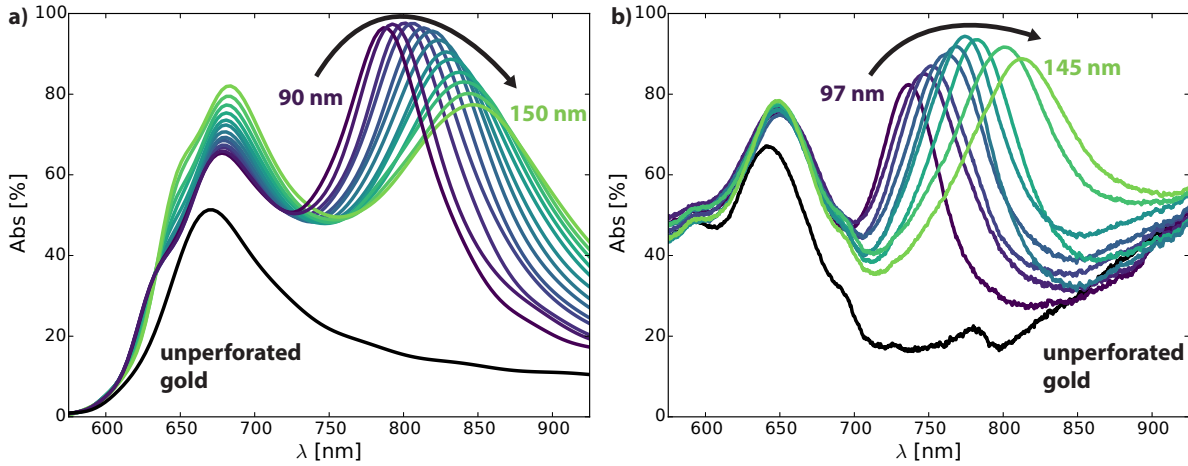


Fig. 3.6: a) Simulated absorption spectra for hole arrays with hole diameters ranging from 90 to 150 nm in steps of 5 nm b) Measured absorption spectra for hole arrays with hole diameters ranging from 97 to 145 nm (see Fig. 3.3c). The black lines represent the absorption of the unperforated gold film.

In order to further confirm the origin of the two characteristic absorption peaks, the electric field intensity normalized to the injected wave is simulated for a cross section through the structure. Fig. 3.7a shows a cross section perpendicular to the injected plane wave at a wavelength of 660 nm. The highest electric field distribution can be found in the Al_2O_3 film. This confirms that the observed absorption peak mainly stems from a Fabry-Pérot resonance which is caused by multiple reflections at gold and silver surface. The resonance position is mainly determined by the thickness of the Al_2O_3 layer. Another indication for this kind of resonance is the fact that an unperforated gold film also shows high absorption at 660 nm (black line, Fig. 3.6a and b).

The electric field intensity distribution at 825 nm, which is the spectral position of the second peak, is shown in Fig. 3.7b. As can be seen from this cross section parallel to the injected plane wave, a strong enhancement of the electric field intensity occurs at the edge of the hole in the gold film.

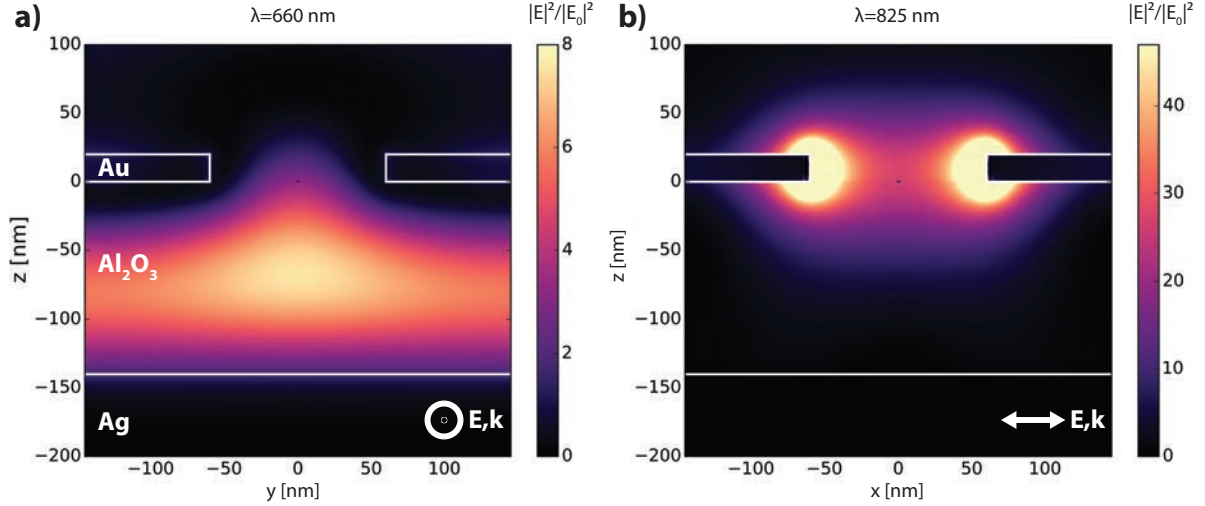


Fig. 3.7: Cross sections displaying the electric field intensity $|E|^2$ with respect to the initial field intensity $|E_0|^2$ for a single unit cell of the plasmonic structure (hole diameter: 120 nm) a) electric field intensity for $\lambda=660$ nm perpendicular to the polarization of the injected plane wave b) electric field intensity for $\lambda=825$ nm parallel to the polarization of the injected plane wave. Note that the color scale in b) is saturated for improved visibility.

3.3 Measure Plasmonic Shifts upon Applied Voltage

The voltage-dependent behavior of the SPP resonance in the nanohole arrays is characterized with the opto-electronic setup which is described in chapter 4. For enhanced capacitance, a diethylmethyl(2-methoxyethyl)ammonium - bis(trifluoromethylsulfonyl)imide (DEME-TFSI, purchased from Sigma Aldrich) ionic liquid is employed. The DEME ion carries a positive charge whereas the TFSI ion carries a negative charge. Initial measurements are performed to characterize the stability of the DEME-TFSI ionic liquid and to test the electrical isolation of the $150 \times 150 \mu\text{m}$ pads. By convention, a negative voltage charges the plasmonic structure with electrons and a positive voltage depletes it of electrons. Fig. 3.8a shows the agglomerated DEME molecule on a contact pad after applying a voltage more negative than -1 V. The TFSI molecule shows stable performance for voltages larger than 2 V. These insights restrict the subsequent measurements for the characterization of the SPP's voltage dependence to the voltage range from -1 to 2 V. Another insight from the local agglomeration of DEME in Fig. 3.8a is that the sample geometry as designed in chapter 3.1 supports sufficient electric isolation between the gold and silver film and between the contacted and surrounding gold. This is further supported by measured $M\Omega$ resistances. The voltage-dependent optical response of the plasmonic structure is then studied with voltage sweeps between -1 and 2 V (starting at 0.5 V, increments of 0.1 V, see chapter 4.1). For different sweeps, the delay times are changed between 0.5 s and 15 s.

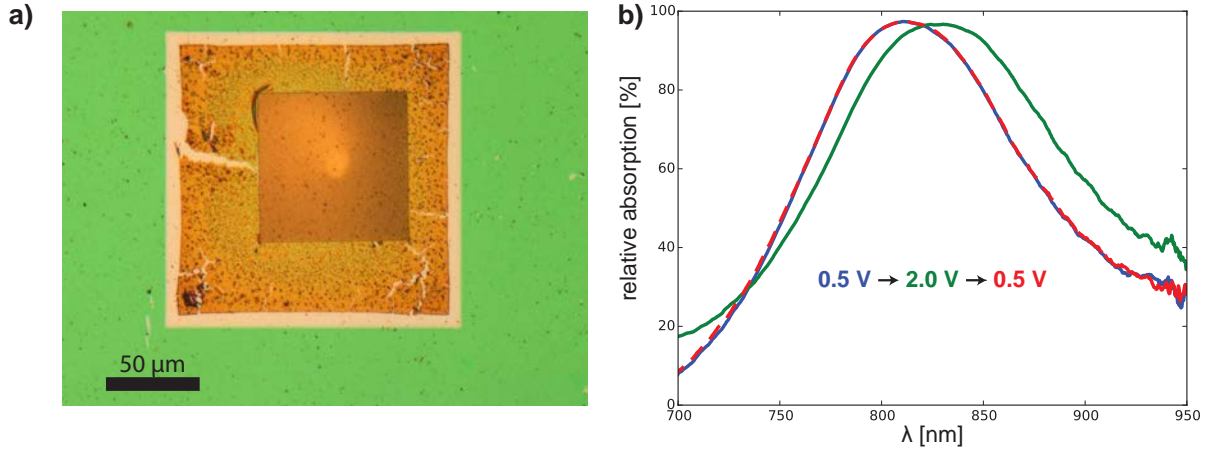


Fig. 3.8: a) Agglomerated electrolyte after applying voltages being more negative than -1 V b) SPP absorption peak at 0.5 and 2 V applied voltage and a delay time of 1 s. At 2 V, a distinct redshift as well as a small reduction in amplitude and a strong broadening of the SPP resonance can be observed. After a full cycle, the original peak position is retained (red line).

Fig. 3.8b displays the SPP peak at 0.5 V and 2 V bias. Changing the applied voltage from 0.5 V (blue line) to 2 V (green line) leads to a distinct and reversible redshift (see red line) and broadening of the resonance.

For a more detailed investigation of the SPP resonance behavior, the peak position as a function of applied voltage is determined from Lorentzian fits to the spectra in energy space (see chapter 4.4). Fig. 3.9 displays the peak positions as a function of voltage for delay times ranging from 0.5 s to 15 s. In the voltage range from -1 V to about 1.2 V, the resonance shows a slight redshift of about 2.5 nm for voltages becoming more positive. Starting at about 1.2 V and reaching to 2 V, the resonance position redshifts significantly by over 10 nm. This observation is in accordance with prior results which found that an onset of the DEME-TFSI's capacitance occurs between 1 and 1.5 V [28] and already suggests that the shift might be largely caused by the plasmonic structure's interplay with the ionic liquid. After the maximum voltage is reached and the applied voltage reduces again, the SPP resonance does not blue-shift immediately but rather shifts more to the red until about 0.5 V where a significant blue-shift occurs. This hysteresis-like behavior can be observed throughout all different delay times where longer delay times show this feature less pronounced. For negative voltages, a hysteresis-like effect does not occur. Also, the maximum observed shift at negative bias has only an amplitude of about 2 nm with respect to zero voltage.

Fig. 3.9 reveals that the redshift of the SPP resonance position is stronger for longer delay times: While for 0.5 s delay time, the difference in peak position between -1 V and 2 V is 11.7 nm, it is 18.2 nm for 15 s delay time. This difference might be explained with a longer settling time for the TFSI layer on the gold surface. Also the hysteresis-like effect reveals a correlation with delay time: At longer delay times, the resonance blueshifts stronger for voltages becoming more negative than for short delay times.

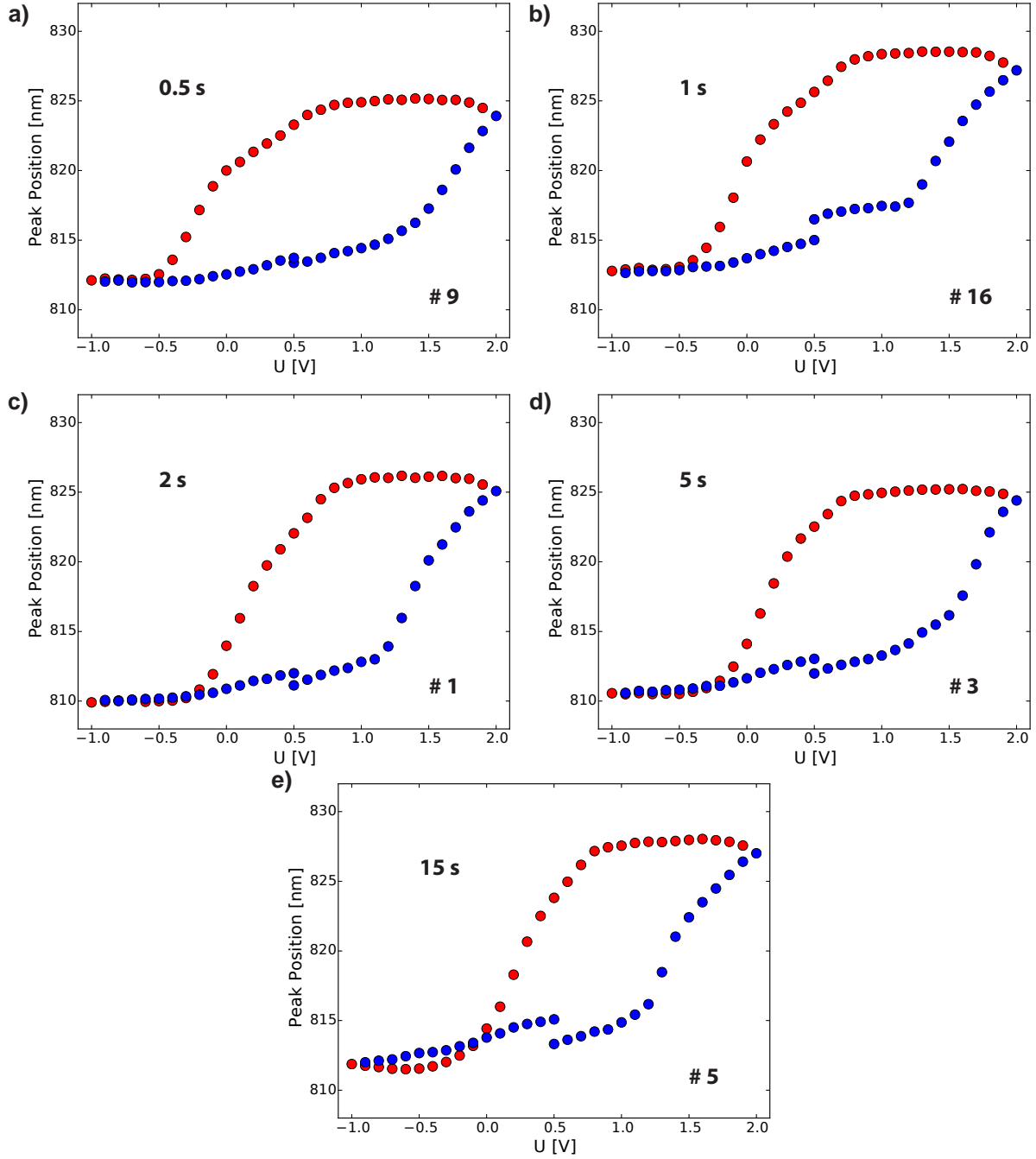


Fig. 3.9: SPP peak positions as a function of applied voltage for delay times of a) 0.5 s, b) 1 s, c) 2 s, d) 5 s, e) 15 s. Blue dots indicate forward and red dots backward directions. The numbers in the bottom right corners indicate the chronology in which measurements were taken and are featured in Fig. 3.11.

Another observation is the behavior of SPP peak width and amplitude as a function of voltage. As for the peak position, a clear hysteresis-like behavior is detected. The peak width is determined from the FWHM of the Lorentzian fit and shows a significant and reversible broadening at more positive voltages. The detected difference in peak width between -1 and 2 V is more than 0.03 eV (corresponds to more than 20 nm, Fig. 3.10a).

Also, the peak amplitude, which corresponds to the maximum value of each Lorentzian fit shows a hysteresis-like effect. Unlike resonance wavelength and width, the amplitude is weakly decreasing for more positive voltages (Fig. 3.10b). Fig. 3.8 shows that the shift in

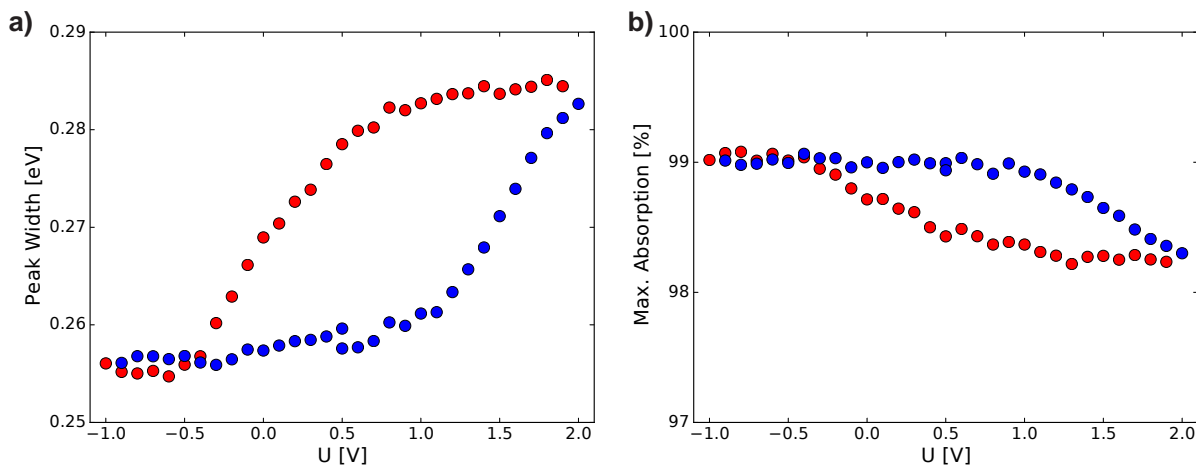


Fig. 3.10: a) SPP peak width for voltages ranging from -1 V to 2 V b) relative SPP peak height for voltages ranging from -1 V to 2 V. The time delay for a) and b) is 0.5 s. Blue dots indicate forward voltages and red dots backward voltages.

SPP peak position is largely reversible. However, it does not state if the reversibility is also given over several measurements. In order to assess this 'actual' reversibility over several cycles, the peak position at zero voltage in forward mode, meaning at the transition from negative to positive voltage is monitored. This procedure excludes as much as possible the influence of hysteresis-like effects. Fig. 3.11 displays the peak position at zero voltage against measurement number and exhibits a slight redshift of about 3 nm over 17 measurements. This behavior could hint at a continuous change of the plasmonic structure, for instance by gradual permanent deposition of TFSI molecules to the gold surface. Remarkably, there is a stronger redshift at measurements 4, 5 and 6 which vanishes with measurement 7. This could be explained with chemisorbed TFSI molecules which randomly detached from the surface between measurement 6 and 7. After this, the general trend of a continuous redshift proceeds. However, to confirm this observation, more measurements are necessary.

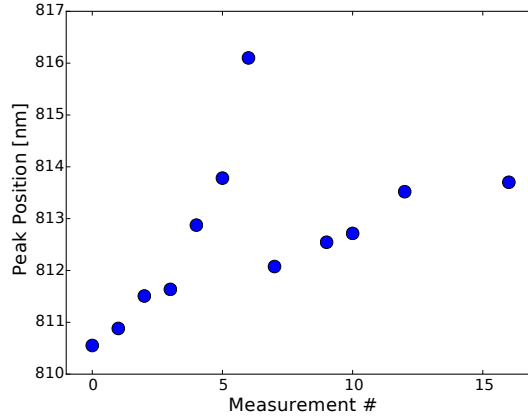


Fig. 3.11: Evolution of SPP peak position throughout multiple measurements. Every data point corresponds to the peak position at 0 V and a transition from negative to positive voltage.

3.4 Modelling Voltage-Induced Plasmonic Resonance Shifts

In the previous section, we reported measured shifts of the SPP resonance as large as 18 nm. Here, we try to deconvolute the contributions of different effects to those shifts. To do so, the electrical properties of the structure and the electrolyte are measured and used to model the SPP response with FDTD simulations. Based on the strong response at positive bias, only the negatively charged TFSI molecule will be considered to understand the optical response of the electron-depleted gold.

The key property of ionic liquids is that the charge-carrying molecules constitute an electric double layer which can be interpreted as a nanoscaled parallel plate capacitor [29]. However, next to this electrostatic contribution to the plasmonic structure's capacitance, another effect - chemisorption of the molecule to the surface - can occur. For DEME-TFSI ionic liquid and DC voltages, it was found that the pseudocapacitance due to ions chemisorbed to the electrode is dominant (about 75%) over the capacitance constituted by the electric double layer (about 25%) [28]. This chemisorption does not occur for AC frequencies above 1 Hz. Based on these findings, we attempt to differentiate between the two contributions by measuring the capacitance in both, AC and DC mode.

3.4.1 Influence of Altered Charge Density in Gold-EDL

In order to only model the contribution of the electrostatic double layer which is formed by the TFSI ions, we estimate the EDL capacitance with alternating current (AC) sweeps at 1 V. For this, a Keysight E4990A Impedance Analyzer is used and set to frequencies ranging from 20 Hz to 1 kHz (Fig. 3.12b). As the samples have a size of only 150 x 150 μm , the influence of the capacitor leakage current and its associated capacitance has to be taken into account by measuring the capacitance with one probe placed in the ionic liquid but not

contacting the sample (Fig. 3.12c). The difference in specific capacitance is shown in Fig. 3.12a and reveals the characteristic behavior of a strongly decreasing capacitance at higher frequencies [28].

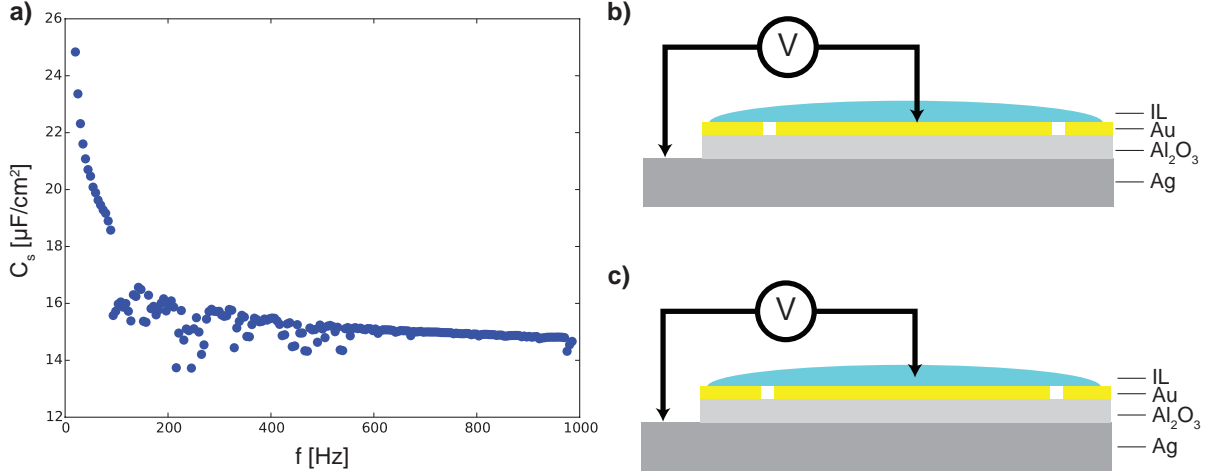


Fig. 3.12: a) Specific capacitance of sample for different frequencies, measured at 1 V. b) measurement in contact mode c) measurement in non-contact mode

In order to understand how charge density alterations in the gold film affect the SPP resonance, we use a Brendel-Bormann model [8] to calculate the altered dielectric function of gold (Eq. 2.6). Modelling of the dielectric function of gold is based on a six-oscillator model and its corresponding parameters (see Table S1) as found by Rakic et al. [7].

To model the change in charge density, the plasma frequency is adjusted with an altered charge density. Any effects that go beyond this classical physics approach, such as changes in the electron wavefunctions are neglected. This strategy has proven to be viable for similar configurations before [17, 21, 30].

$$\omega_p'^2 = \frac{n'e^2}{m^*\epsilon_0} = \frac{n'}{n_0}\omega_p^2 \quad (3.1)$$

Here, n' is calculated from an extrapolation of the specific capacitance measured at 1 V (see Fig. 3.12a) and n_0 is the charge density of uncharged, bulk gold ($5.9 \times 10^{28} \text{m}^{-3}$). On basis of the calculated relative change in charge density n'/n_0 (Table S2), the real and imaginary part (ϵ_r and ϵ_i) of the dielectric function can be recalculated and fed into the FDTD simulations. As metals do not exhibit an extended space charge layer but concentrate all free charges on their surface [31], we attempt to take this effect into account for our model. The first model that we apply is assuming a 0.5 nm thick layer with altered dielectric functions (see Fig. 3.13a). This accounts for the fact that free charges accumulate in one or two single atomic layers [32]. In the second model, we consider a 5 nm thick layer (Fig. 3.13b) of altered charge density to verify the procedure [21]. The benefit of a 5 nm thick layer of altered charge density is that the relative change in charge density (2.1 %) is smaller than for the case of a 0.5 nm thick layer (21.2 %). The recalculated dielectric functions of gold are displayed in Fig. 3.13c and d. It can be seen that the perturbation of the gold's dielectric functions is weaker in the case of a 5 nm thick layer. Moreover, the minimum mesh size around the

charge layer which is used in the simulation is larger and thereby more trustworthy (0.2 nm instead of 0.05 nm in z-direction). The simulated shift of the SPP peak position for a 0.5 nm and a 5 nm thick layer of altered charge density is shown in Fig. 3.13e. Both models yield approximately the same result and predict a maximum shift of about 1.7 nm at 2 V. Due to this result, we will only consider the model with a 5 nm thick layer in the following.

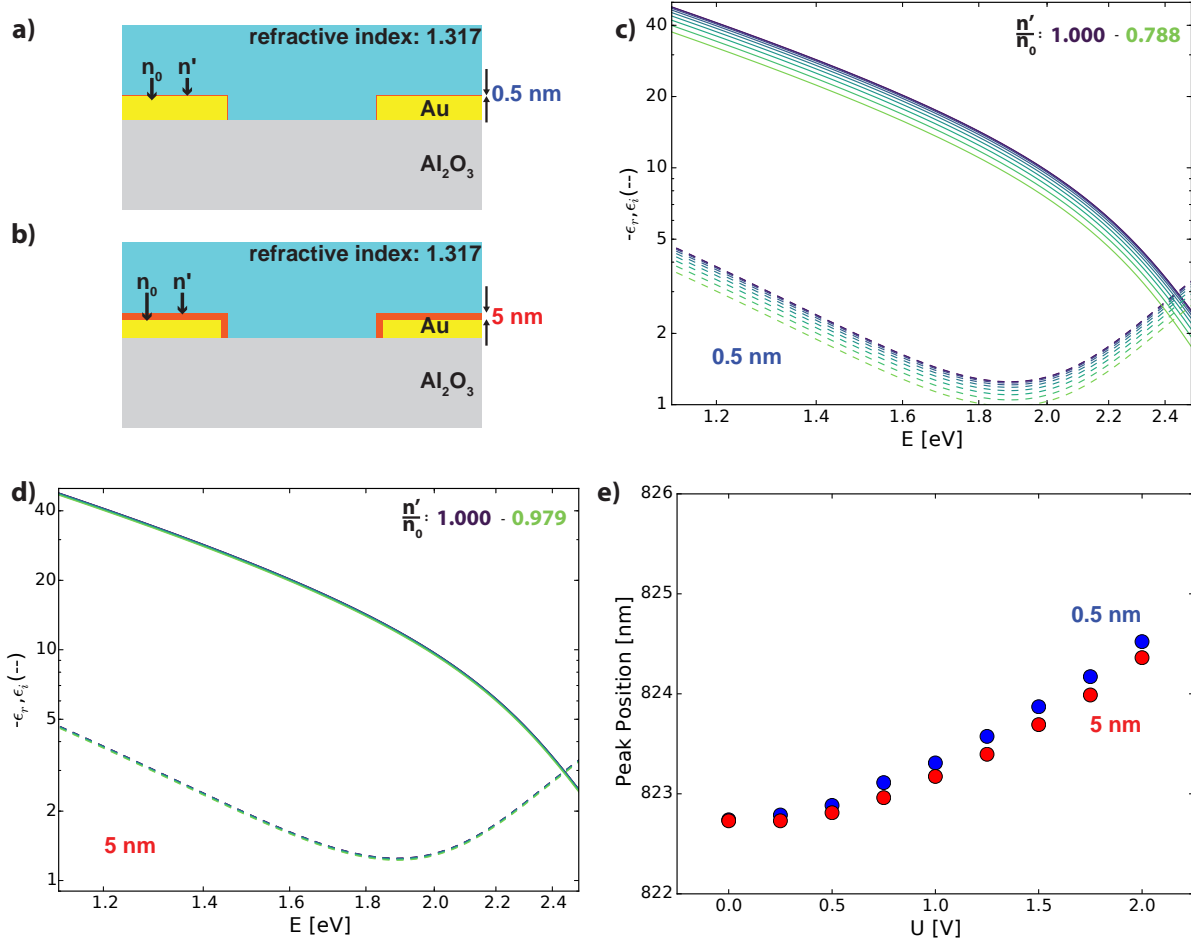


Fig. 3.13: a), b) Schematic cross sections of the FDTD environment around the gold layer for a 0.5 nm and 5 nm thick layer (orange) of altered charge density, respectively c) altered dielectric function for a 0.5 nm thick layer of altered charge density with n'/n_0 ratios varying from 1.000-0.788 d) altered dielectric function for a 5 nm thick layer of altered charge density with n'/n_0 ratios varying from 1.000-0.979 e) simulated peak positions for 0.5 nm (blue) and 5 nm (red) layer of altered charge density, simulated with the dielectric functions from c) and d), respectively.

3.4.2 Influence of Refractive Index Change in Ionic Liquid

When the ionic liquid contributes capacitance to the gold film, this means that the charged molecules in the liquid assemble close to the sample's surface and thereby also change the refractive index in its vicinity. This behavior of ionic liquids can be described with a Helmholtz double layer model [33] which assumes that all charged molecules essentially form a parallel plate capacitor with a thickness of molecular dimensions with the metal surface.

Based on this model, we assume that the refractive index of the ionic liquid is only altered within the Helmholtz double layer (see inset of Fig. 3.15a). This refractive index change can be estimated with the Lorentz-Lorentz equation which expresses the refractive index as a function of molecular polarizabilities α_i and number densities n_i (Eq. 2.11).

To do so, the molecular polarizability of TFSI (see Fig.3.14a) molecules is determined according to the method of Kang and Jhon [15], using the parameters found by Miller (Fig.3.14a) [34]. This method is based on the additivity of atomic hybrid polarizabilities of single atoms to a molecular polarizability. For the TFSI molecule, this yields a molecular polarizability of $\alpha_{\text{TFSI}} = 13.2 \text{ \AA}^3$. As the TFSI molecule in the case of the ionic liquid is negatively charged, the actual polarizability is expected to be even higher. This will not be further considered.

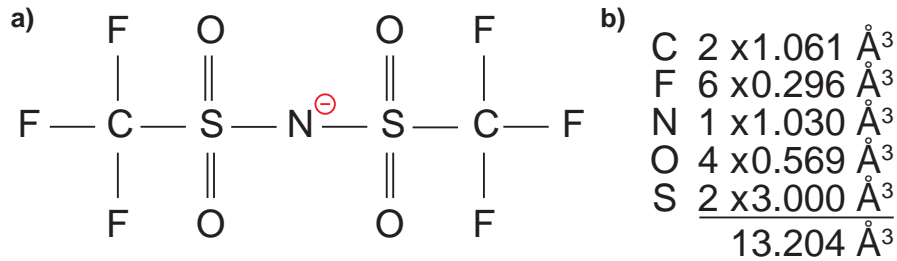


Fig. 3.14: a) Chemical structure of bis(trifluoromethylsulfonyl)imide (TFSI) molecule with negatively charged nitrogen atom in the center b) molecular polarizabilities of the separate atoms and total molecular polarizability of TFSI molecule according to [34]

Based on the assumption that every TFSI molecule carries one charge carrier, the number of TFSI molecules needed for the specific capacitances (see Table S3) can be calculated

$$N_{\text{TFSI}} = \frac{C_s \cdot U}{e} \quad (3.2)$$

Assuming that all these molecules are in a double layer with a thickness of 8 nm, which corresponds to the average height of a TFSI molecule [35], the areal number density of TFSI is

$$n_{\text{TFSI}} = \frac{N_{\text{TFSI}}}{8 \text{ nm}} \quad (3.3)$$

From the number density of water ($n_{\text{H}_2\text{O}} = 33.3 \cdot 10^{27} \text{ m}^{-3}$), the number of water molecules contained by a volume of 8 nm thick layer can be calculated. Based on the van der Waals volume of TFSI (156.7 \AA^3 [36]) and water (19.5 \AA^3 [35]), the new number density of H_2O molecules in the 8 nm layer can be estimated as

$$n'_{\text{H}_2\text{O}} = n_{\text{H}_2\text{O}} - \frac{V_{\text{TFSI}}}{V_{\text{H}_2\text{O}}} \cdot n_{\text{TFSI}} \quad (3.4)$$

The calculated refractive index as a function of voltage is implemented in the FDTD simulations. From this, the Fig. 3.15a shows the simulated change in SPP peak position as a function of voltage for altered refractive index near the surface of the gold film. It indicates that the altered refractive index near the surface contributes about 0.7 nm to the observed shift.

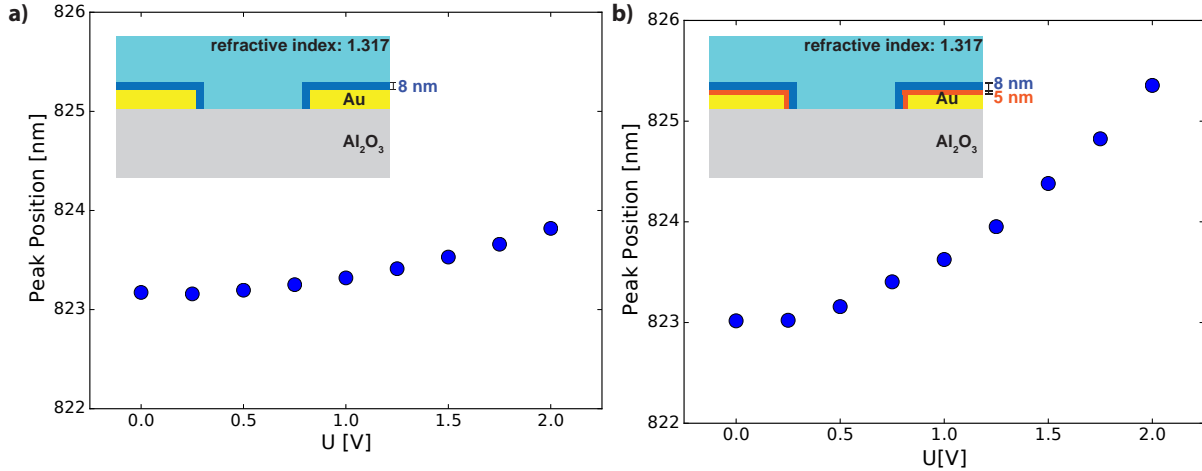


Fig. 3.15: a) Simulated peak positions for a 8 nm thick layer of enhanced refractive index b) simulated peak positions for a 8 nm thick layer of enhanced refractive index and altered charge density in a 5 nm thick layer. Insets: schematic cross sections of the FDTD environment for a) and b), respectively.

In the next step, the combined influence of altered dielectric function in the gold layer and the change in refractive index in the ionic liquid is modeled in FDTD (see inset of Fig. 3.15b) and the result is shown in Fig. 3.15b. The predicted shift due to the electrostatic double layer of TFSI is 2.3 nm. This means that about two thirds of the shift are due to altered charge density and about one third is due to altered refractive index. Adding up the sole contributions of these two effects leads to a slight overestimation of the total shift.

3.4.3 Influence of Chemisorption

The second main contribution to the measured shift of the SPP resonance stems from the pseudocapacitance of a TFSI layer which is adsorbed onto the gold surface. In order to estimate the amplitude of this effect, we follow a similar route as in chapter 3.4.1 and 3.4.2. The capacitance of the parallel-plate capacitor in connection with the DEME-TFSI electrolyte was again measured with a Keysight E4990A Impedance Analyzer. This time, a DC bias sweep from -1 V to 2 V in 50 mV increments (20 Hz, 5 mV) was performed to determine the specific capacitance of a $150 \times 150 \mu\text{m}$ field on the sample. Again, the specific capacitance of the open circuit is used to take into account the leakage current. In Fig. 3.16a it can be seen that the specific capacitance strongly increases for positive voltages to a maximum value of $429 \mu\text{F}/\text{cm}^2$. In this configuration, the gold film is on a positive potential and the TFSI molecule contributes to the capacitance. The strong increase of specific capacitance at 1 V corresponds well with the optical measurements in which a strong change in peak position and shift occurred for voltages above 1.2 V (see Fig. 3.9 and 3.10). The unexpected decrease of specific capacitance between 1.7 and 2 V shows the limitations of this measurement approach which possibly arise from the fact that the leakage currents in contact and non-contact mode are dominant over the capacitance of the device.

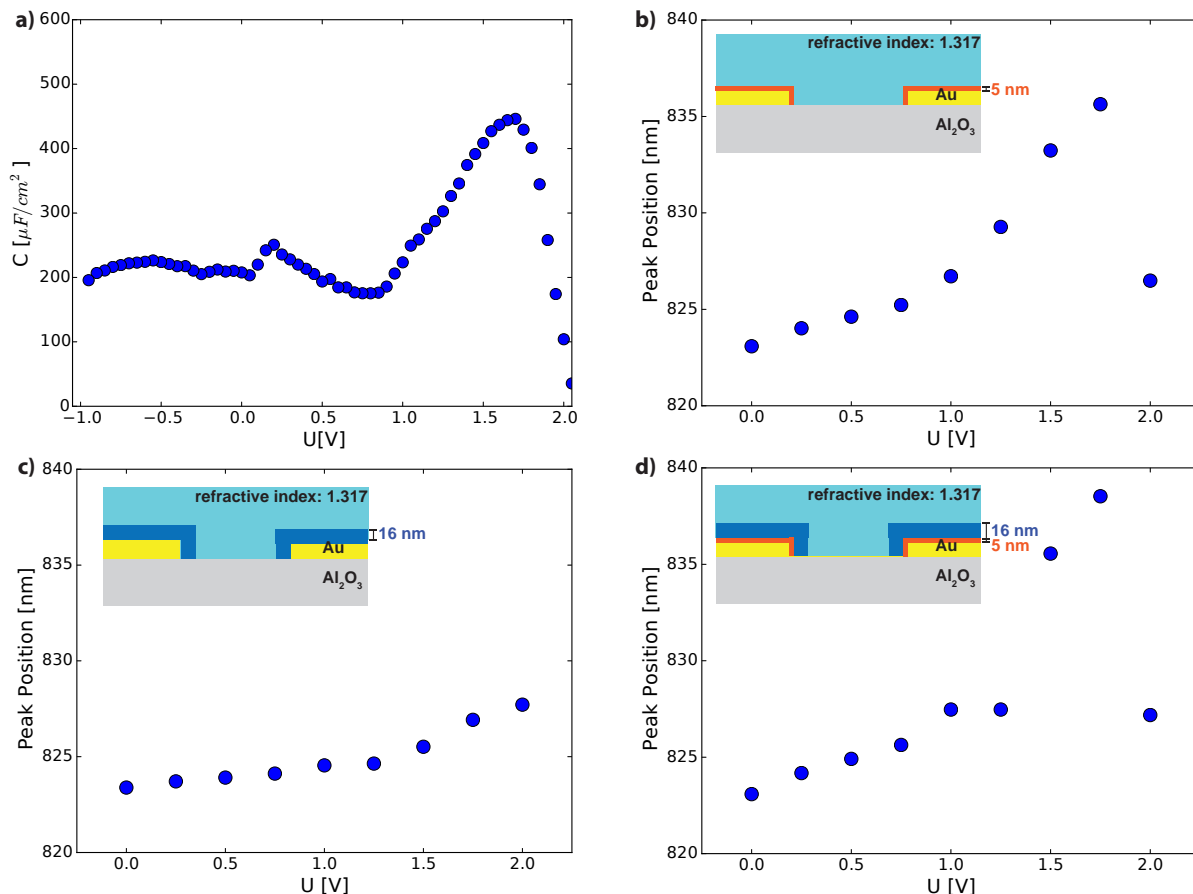


Fig. 3.16: a) DC specific capacitance of sample, corrected for leakage current b) simulated peak positions for charge 5 nm (red) and 20 nm (blue) layer of altered charge density c) simulated peak positions for a 16 nm thick layer of enhanced refractive index d) simulated peak position for a 16 nm thick layer of enhanced refractive index and altered charge density in a 5 nm thick layer. The insets depict the respective simulation environments in FDTD.

Analogously to the procedure in chapter 3.4.1, the altered charge density in the gold film is calculated (see Table S4). The charge corresponding to the highest measured capacitance surpasses the intrinsic charge in a gold layer of 0.5 nm thickness. Therefore, we adjust the model and only consider a 5 nm thick layer of altered charge density (see inset of Fig. 3.16b). The simulated shift of the peak position from voltages changing from 0 to 2 V are displayed in Fig. 3.16b: As expected from the strongly enhanced (pseudo-) capacitance, the shift is much stronger and amounts to about 12.5 nm between 0 and 1.75 V.

Just as for the charge density, we follow the same procedure for the influence of altered refractive index of the ionic liquid in the vicinity of the gold layer (compare chapter 3.4.2). Due to the higher capacitance, we assume that the TFSI molecules assemble in a 16 nm instead of a 8 nm thick layer at the surface (see inset of Fig. 3.16c). With this model, this layer will not be completely depleted of H₂O molecules but by more than two thirds at the highest capacitance (see Table S5). The resulting change in peak positions in dependence of applied voltage is depicted in Fig. 3.16c and predicts a contribution of about 4.5 nm to the shift.

The combined influence of altered charge density and refractive index near the surface is

shown in Fig. 3.16d and yields a maximum shift of 15.5 nm. As for the simulations for the electrostatic double layer in chapter 3.4.1 and 3.4.2, the combined effect is slightly smaller than the sum of the contributions of refractive index change near the surface and change of charge density in the gold.

While our model reproduces the observed shifts of the SPP resonance well, the peak broadening cannot be observed. In contrast, even a trend of slight decrease in peak width is simulated for more positive voltages (see Fig. 3.17a). Also, the simulations yield a slight increase in peak amplitude for higher voltages (See Fig. 3.17b). This is again in contrast to slightly decreasing amplitudes in the measurements.

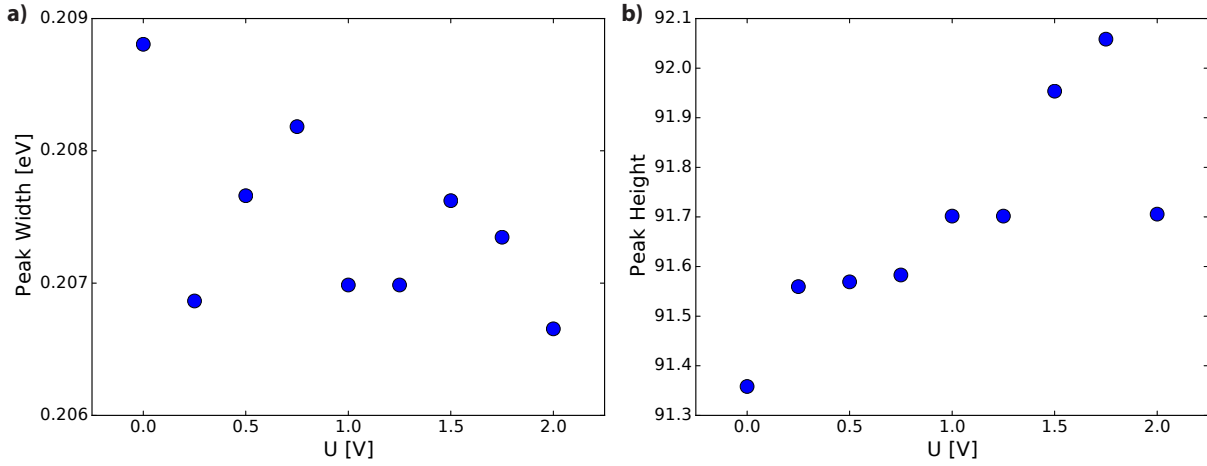


Fig. 3.17: a) Simulated change in peak width and b) peak amplitude as a function of voltage for changed refractive index in the ionic liquid and altered charge density in a 5 nm gold layer (see inset of Fig. 3.16d).

3.5 Discussion

The observed shifts of the SPP resonance wavelength are to our knowledge the first demonstration of charge-induced plasmon resonance manipulation in a continuous metal film and not in nanoparticles. The magnitude of the measured shifts, which reaches 18.2 nm, is about the same as the maximum shift that was observed for silver nanoparticles in a cationic polymer matrix [18]. Electrochemical characterization of the interplay between gold film and ionic liquid suggest that two processes, a fast electrostatic double layer formation and a slow chemisorption of ions to the surface are responsible for the structure’s voltage-dependent optical response. When including the measured capacitances in FDTD simulations, the amplitude of the measured shifts can qualitatively be confirmed: In our model, an electrostatic double layer forming at the gold surface predicts a shift of about 2.5 nm of which about two thirds can be attributed to a change in the gold’s charge density and to one third to a local change of the ionic liquid’s refractive index. The main contribution to the observed shift stems from the pseudocapacitance provided by TFSI molecules which are chemisorbed to the gold surface and donate their ionic electron. The onset of a strong increase of the specific capacitance due to chemisorption at about 1 V corresponds well with the strong shift of the SPP resonance for voltages above 1.2 V. The observed chemisorption behavior is in accordance with prior studies on the TFSI molecule [28].

The accuracy of our model is mainly limited by the quality of capacitance measurements which are dominated by the contributions of leakage currents. Another uncertainty stems from the models which are employed for the alteration of the refractive index in the ionic liquid and of the gold’s dielectric function. In reality, the accumulation of ions near a metal’s surface can rather be described with a combination of the compact Helmholtz-layer and a diffuse layer extending over several tens of Å (Gouy-Chapman-Stern model) [33]. Moreover, the Lorentz-Lorenz equation which was used to describe the optical response of the ionic liquid only calculates the real but not the imaginary part of the refractive index. This means that possible absorption processes in the ionic liquid are not taken into account in the simulations.

The Brendel-Bormann model which is used to describe the gold’s dielectric function is based on a fit to dielectric data obtained from bulk gold and not exactly from a ultrathin film of only 20 nm thickness. Although it is possible to fabricate ultrathin gold films with the same optical properties as bulk gold [9], there still might be some deviations. Moreover, the assumption of altered charge density displaying the sole contribution to the change of dielectric function does not consider any changes of the damping constant and in the gold’s electronic structure. As the damping constant is dependent on the lifetime of electron-electron interactions, it is likely that charge density variations also change the damping constant.

Also the fact that our FDTD simulations predict a reduction of peak width for more positive voltages instead of the measured increase of about 20 nm suggests that changes in the damping constant should be taken into account. Also for the peak amplitude, simulations predict a slight increase which is in opposition to the experimental data. A possible route to model the peak broadening and amplitude decrease could be to adjust the damping parameter in the Brendel-Bormann model. It can be assumed that the electron-electron scattering

is dependent on charge density [37]. One could account for this by introducing an additional damping term $\Gamma_{\text{alter}}(n)$ to the damping constant such that

$$\Gamma' = \Gamma_0 + \Gamma_{\text{alter}}(n) \quad (3.5)$$

However, it would be difficult to estimate $\Gamma_{\text{alter}}(n)$ from measurements. One could rather try to optimize this parameter such that the desired result occurs [17].

Another effect which could contribute to the broadening of the resonance peak could be adsorbate damping due to unoccupied states in the TFSI molecule. These states, which are located above the Fermi level of metals can be occupied and thereby reduce the absorption amplitude and broaden the resonance [38]. However, this effect is not further investigated in our study.

We attribute the observed hysteresis effect with its strong time-dependence to the delayed detaching of TFSI molecules from the surface. Unlike in a similar study which employed a NaCl-based electrolyte [21], we are not able to observe a quasi-vanishing of the hysteresis effect for slower cycling. A possible explanation for this could be that the comparably high mass of TFSI molecules inhibits the detachment from the surface.

3.6 Conclusions

We successfully fabricated a plasmonic structure featuring nanoholes in an ultrathin gold film. By stacking this film onto Al_2O_3 and silver backmirror, the absorption properties can be greatly improved and a platform for electrical measurements is created. Subsequently, optical measurements and FDTD simulations are employed to study the dependence of the SPP resonance on geometric properties such as hole diameter, pitch and thickness of Al_2O_3 and gold layers. Measured and simulated spectra show good agreement with respect to amplitude, shape and spectral position of the SPP and Fabry-Pèrot resonance.

In a next step, opto-electrical measurements were performed to characterize the dependence of the SPP resonance on applied voltages. The response is enhanced by employing an ionic liquid which increases the structure's capacitance. In dependence of the delay time between voltage change and recording of the spectrum, reversible shifts of the SPP resonance ranging from 11.7 to 18.2 nm can be observed. Moreover, a distinct broadening and a weak amplitude decrease of the SPP resonance can be observed for higher voltages.

On basis of frequency-dependent capacitance measurements, we recalculated the dielectric function of gold and the refractive index in the ionic liquid. Subsequent FDTD simulations, which incorporated these altered properties enabled us to quantitatively reproduce the measured shifts of the SPP resonance.

We find that the chemisorption and its associated pseudocapacitance are the main contributor to the observed tuning effect. The influence of the electrostatic double layer of ionic molecules in contrast is only noticeable as the weak shift for voltages below the onset of chemisorption at 1.2 V. From the disentangled effects of altered charge density in the gold and a changed refractive index of the ionic liquid, we determine that the former contributes about three quarters and the latter about one quarter to the observed shifts.

The simulated trends for SPP resonance width and amplitude are opposite to the experi-

mental results but are likely to be reproduced by adjusting the electrons' damping constant to the reduced charge density.

3.7 Outlook

Our study shows that for a full comprehension of a plasmon's response to externally applied potentials also the changes in the local refractive index have to be taken into account. These insights might help to better understand plasmonic sensors measuring adsorption events. Moreover, the investigated structure with its strong absorption in a limited bandwidth could enable the construction of tuneable notch filters.

A general limitation of the investigated experimental system is that it is mostly suitable for DC measurements because of the strong frequency-dependence of the TFSI's behavior. Moreover, the amplitude of the observed SPP resonance shift largely relies on the pseudo-capacitance of chemisorbed ionic molecules. A possible route to overcome these problems could be to employ another kind of ionic liquid which can supply considerable electrostatic capacitance at higher frequencies. For a more stable experimental system, one could even consider ionic gels. Such gels typically consist of a mixture of ionic liquid with a polymer and were shown to have specific capacitances of about $10 \mu\text{F}/\text{cm}^2$ at kHz frequencies [39]. For a more accurate measurement of the SPP resonance position as a function of altered metal charge density it would be worth to consider an experimental design which works without any kind of electrochemical capacitance enhancement. This has the benefit that one does not have to deal with the coupled effect of refractive index change in the metal's vicinity and dielectric function change in the metal. In this case, the only capacitance would stem from the parallel plate capacitor which is constituted by the $\text{Au} - \text{Al}_2\text{O}_3 - \text{Ag}$ -layer structure which amounts to only $0.05 \mu\text{F}/\text{cm}^2$. A way to measure the effect of the minute charge deviations which can be realized with such a parallel plate capacitor architecture could be to carry out an AC experiment where the optical response is coupled to an oscillating voltage via a lock-in amplifier. The high sensitivity of lock-in amplifiers could even make the optical detection of single electrons possible.

Another option to electrically tune the SPP resonance could be to take advantage of the electro-optic effect. This effect describes the change of refractive index in a dielectric upon applying strong electric fields. A possible realization would be to replace the Al_2O_3 -layer with a transparent material which supports the electro-optic effect [40]. A candidate for this could be lithium niobate which has been shown to exhibit strong electro-optic alterations of refractive index [41].

Chapter 4

Building an Opto-Electronic Microscope

Experimentally detecting charge-induced changes of the SPP resonance position demands for an optical microscopy setup which allows to measure the plasmonic structure's optical response in dependence of applied voltages. For this reason, an opto-electronical setup is built. Fig. 4.1 is a photograph of the setup and Fig. 4.2 displays the setup schematically. Optical measurements are performed using the light of a supercontinuum laser (Fianium) whose light beam is targeted onto an angled glass plate to strongly reduce the intensity by using only the reflection (about 4%) in the further beam pass. To attenuate the beam power even more, neutral density filters are employed so that the final beam power reaching the sample is about 400 nW.

In order to reach a near-to diffraction limited spot, the back-aperture of the objective has to be filled by the beam as much as possible. This is achieved by expanding the laser beam with two achromatic lenses which are built in a Keplerian telescope configuration. For magnifying purposes, the first lens L1 has a smaller focal length (10 mm) than the second one (L2, 80 mm). The ratio of the focal lengths determines the magnification of the telescope and is for the chosen set of lenses $80\text{mm}/10\text{mm}=8$. For a parallel beam, the distance between the lenses has to be chosen such that it is the sum of their focal lengths, namely 90 mm. An iris diaphragm ID between the lenses is used to cut off non-symmetrical parts of the beam.

Because of the liquid electrolyte used in the experiments, the objective has to be mounted vertically and hence the beam passes a periscope before going through the objective. The mirrors M4-M6 in this periscope have to be adjusted such that the beam hits the the back aperture of the objective perpendicularly.

For focusing the light onto the sample, a 20x objective (Mitutoyo, WD=20 mm, NA=0.40, infinity-corrected) which is optimized for the near-infrared is used. Its long working distance allows to apply ionic liquid and place electrical probes on the sample. The reflected signal is passed through a pellicle beamsplitter (PBS, 700-900 nm, 45:55 (R:T)) and a 200 mm achromatic lens which focuses onto an 105 μm core fiber connected to a spectrometer (PI Acton SpectraPro 2300i). The benefit of using a pellicle beam splitter is that unlike the cube version, it does not show ghost reflections.

Imaging of the sample is achieved by illuminating the sample with a broadband LED which is coupled into the beampath with a cube beamsplitter (CBS, 700-1100 nm, 50:50 (R:T)). For

reasons of visual clarity, the LED beam is not coupled into the beampath. Switching between spectroscopy mode and imaging mode is achieved with a mirror on a flip mount (M1) which projects the reflected image onto a CMOS sensor (Thorlabs DCC1645C). The mirrors M1 and M2 can be used to adjust the beam position on CMOS sensor and spectrometer, respectively.

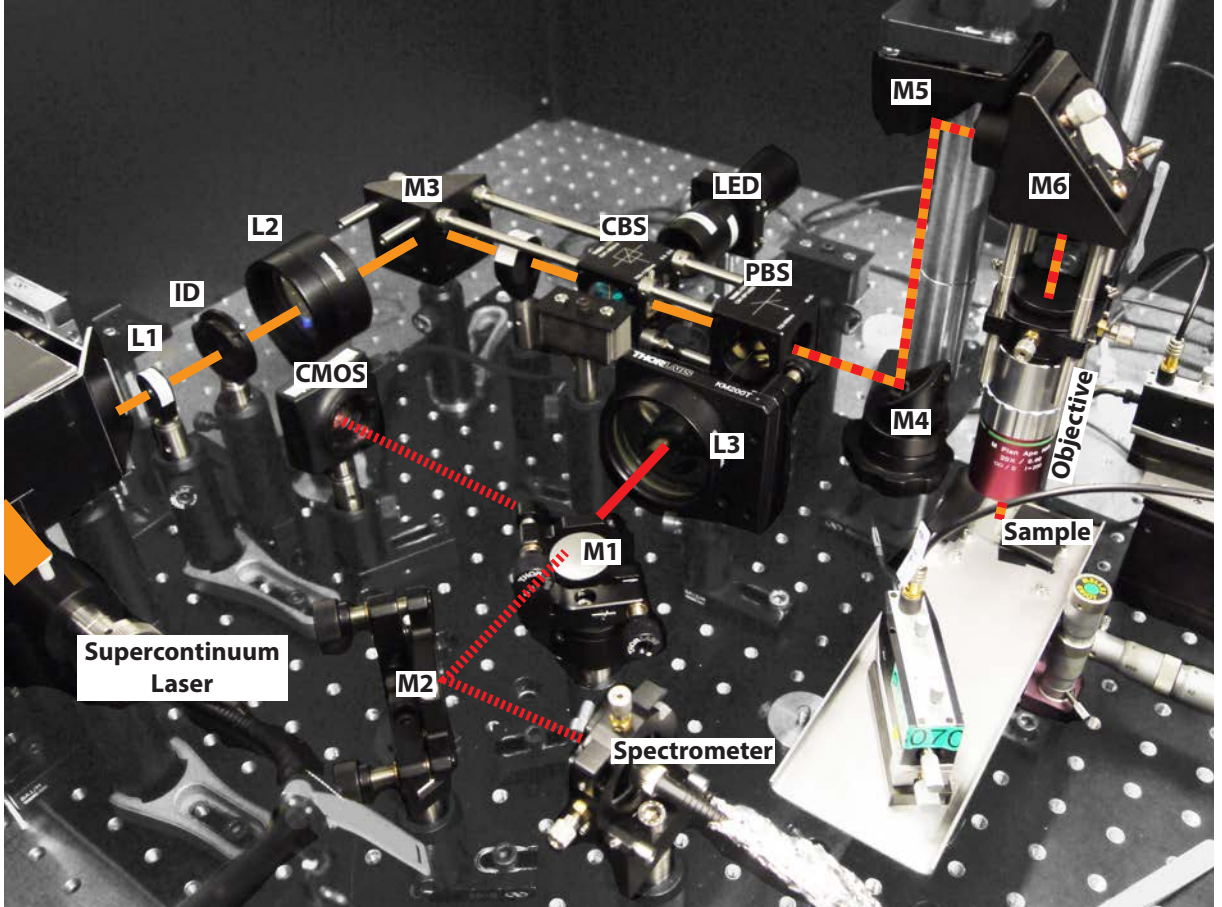


Fig. 4.1: Photograph of the setup. The orange line represents the probe beam of the laser and the red line the beam reflected off the sample. Schematic of the opto-electronic setup that is used for sample characterization. The key elements are labeled: L1 and L2 are the lenses constituting the beam-expanding telescope; the iris diaphragm ID cuts off non-symmetrical parts of the beam; L3 is the lens focusing onto either the CMOS-camera (with mirror M1) or the spectrometer (with mirror M2); a cube beamsplitter (CBS) is used to couple the LED light into the beam path (not displayed for visual clarity) and a pellicle beamsplitter (PBS) which divides between probe and detection beam path. M3-M6 are steering mirrors. The dotted orange lines behind M1 indicate imaging and spectroscopy mode, respectively.

The sample is placed on a xyz-translation stage which supports 8 mm travel in either dimension with an accuracy of 1 μm .

Electrical contact to the sample is made via 7 μm tungsten probes (American Probe & Technologies) connected to a source measure unit (Keithley 2612) which can be used to apply a potential to the sample.

The ground probe (connecting to silver backmirror) rests on the sample stage whereas the second probe which contacts single devices is on a second xyz-translation stage (see Fig.

4.4). This has the merit that the probe can be positioned relative to the objective and thus does not need any more lateral adjustments.

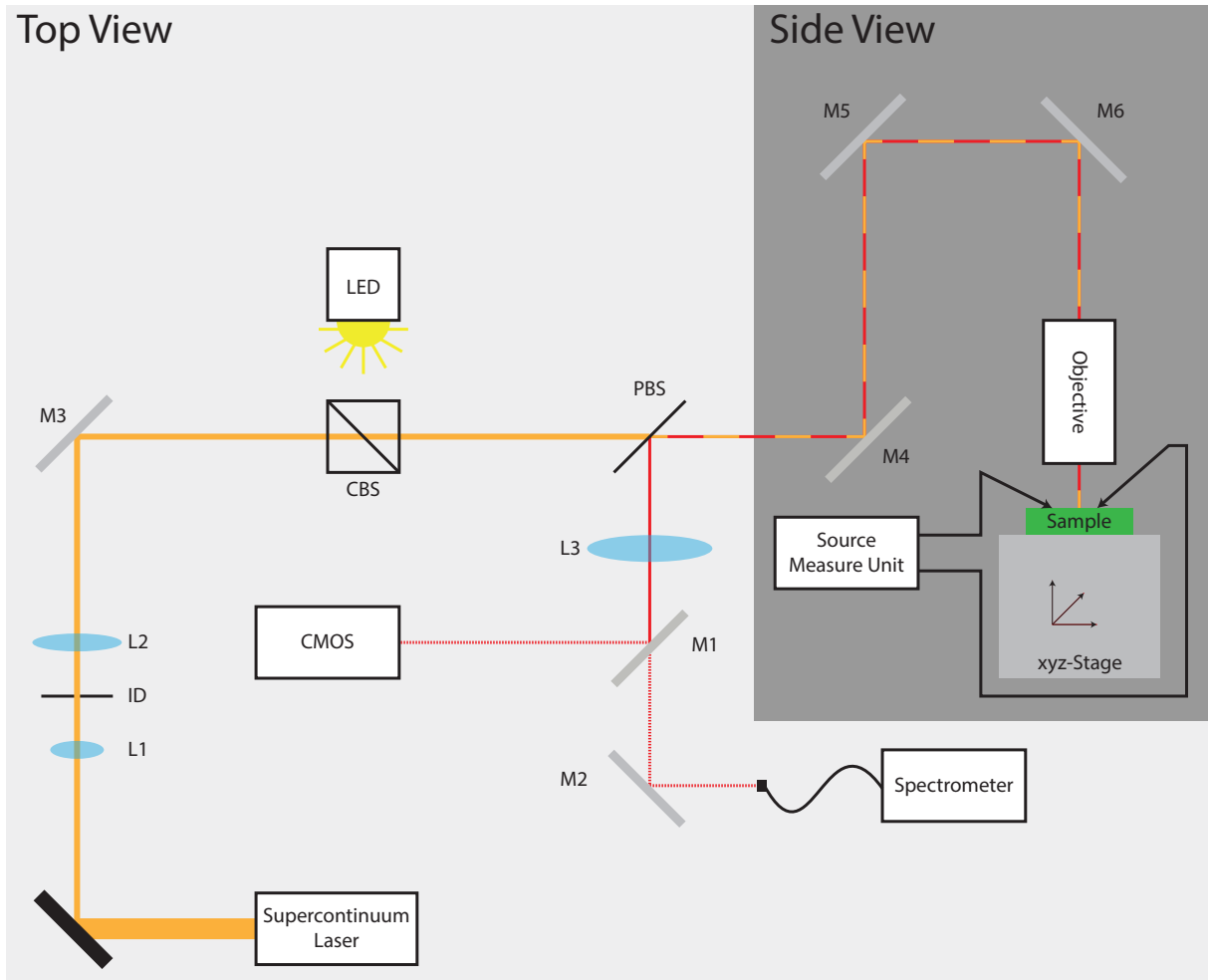


Fig. 4.2: Schematic of the opto-electronic setup that is used for sample characterization. The orange line represents the probe beam of the laser and the red line the beam reflected off the sample. The key optical elements are labeled: L1 and L2 are the lenses constituting the beam-expanding telescope; the iris diaphragm ID cuts off non-symmetrical parts of the beam; L3 is the lens focusing onto either the CMOS-camera (with mirror M1) or the spectrometer (with mirror M2); a cube beamsplitter (CBS) is used to couple the LED light into the beam path (not displayed for visual clarity) and a pellicle beamsplitter (PBS) which divides between probe and detection beam path. M3-M6 are steering mirrors. The dotted orange lines behind M1 indicate imaging and spectroscopy mode, respectively.

4.1 Software

Measurements are undertaken with a home-built software which controls the spectrometer as well as the source measure unit. A basic measurement, which is schematically displayed in Fig. 4.3, assembles of a loop from a start voltage to a maximum voltage back over the start voltage to a minimum voltage and then finishing at the start voltage. The voltage increment ΔV can be chosen as well as the number of measurement cycles that are recorded. In a next step, a time delay t_d between altering the voltage and taking the spectrum can be chosen. The settings for recording the spectrum are implemented via a software interface to WinSpec, the default measurement software for PI Acton spectrometers. Most importantly, the shutter setting, region of interest (ROI) and exposure time t_{exp} can be chosen.

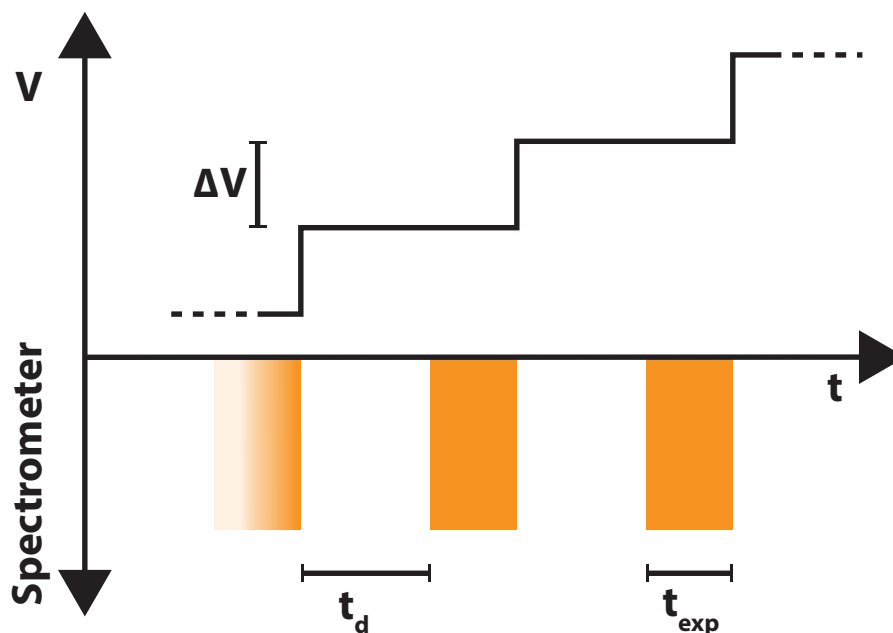


Fig. 4.3: Schematic of a chronological sequence during a standard measurement performed with the opto-electronic setup. The upper half space displays the voltage as it is gradually changed in increments of ΔV . The lower half space displays the status of the spectrometer with orange standing for exposure with a duration of t_{exp} and white for no exposure. t_d is the delay time between voltage change and opening of the spectrometer shutter.

4.2 Performing Measurements with the Setup

The first step in running measurements with the setup is to take a reference measurement, preferably on silicon. Then, the samples which were described in chapter 3.1 can be placed under the objective. When it is ensured that the lateral travel of the translation stage is sufficient to reach all devices on the sample, the sample is fixed to the translation stage with adhesive tape. After the sample is brought to focus, a pipette can be used to apply the ionic liquid, if necessary. Subsequently a hole array is parked under the laser spot and electrical contact can be made with the device: For that, one of the probes (Probe I, Fig.

4.4) is connected to the silver backmirror by scratching on the margin of the sample. The second probe (Probe II, Fig. 4.4) demands for a more precise positioning which is achieved by locating it in the field of view. Subsequently, the probe can be lowered to the sample with the z-actuator of the probe-stage. Contact to the gold is reached when the probe's apex reaches focus. By monitoring the resistance between the probes, it can be ensured that the sample is not shorted.

For all measurements described in this thesis, the 150/800 nm blazed grating was selected and set to 800 nm center wavelength. Moreover, the exposure time of the spectrometer was set to 0.2 s.

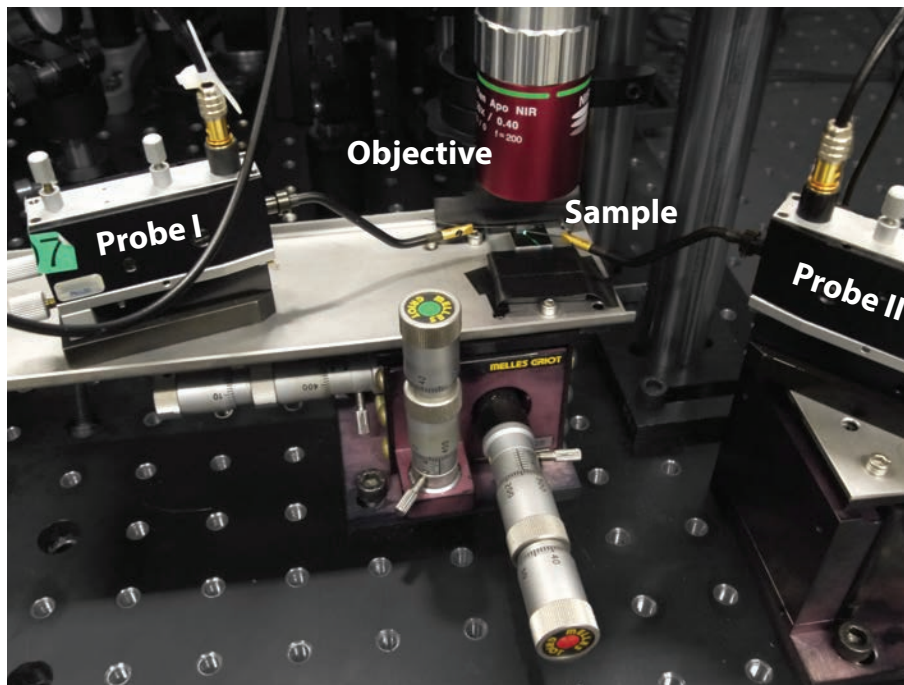


Fig. 4.4: Photograph of the setup during a measurement: Probe I contacts the Ag backmirror and has a fixed position relative to the sample. Probe II is positioned on a separate translation stage which allows a fixed position relative to the objective. This probe is lowered to contact the gold.

4.3 Characterization of the Setup

The measured intensity on the spectrometer depends on how much the sample is in the focus of the objective. Another parameter which might deteriorate the quality of measurements is the alignment of the mirrors in the periscope. If these mirrors are not aligned such that the beam traverses the back aperture of the objective perpendicularly, the reflected signal moves over the fiber of the spectrometer as the objective-sample distance is changed. The influence of these convoluted effects can be estimated by comparison of the measured signal in dependence of sample height. For this, the signal reflected from a silicon substrate is investigated. Fig. 4.5a shows the relative deviation in measured intensity δI as a function of wavelength for measurements taken with $\pm 2 \mu\text{m}$ height alteration of the sample from the maximum signal intensity. δI is on average below 2 % in the region of main interest between

700 and 900 nm which is acceptable for the kind of measurements that are performed with the setup. Fig. 4.5b-d show micrographs of the laser spot on the silicon substrate for different heights. As it can be seen, the spot shape and position on the sample does not greatly change for the different heights.

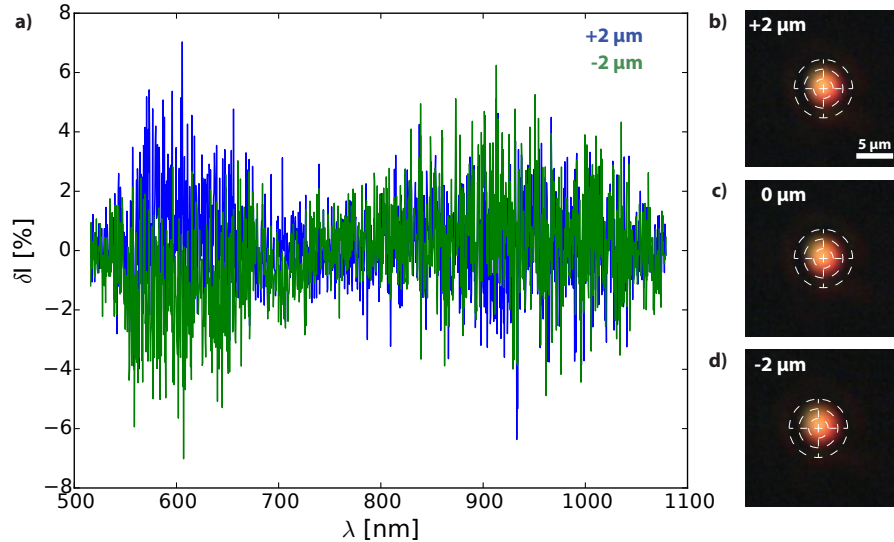


Fig. 4.5: a) Relative change in measured intensity for deviations of $\pm 2 \mu\text{m}$ from ideal focus b-d) micrographs of the laser spot on for deviations from the focus of $+2$, 0 and $-2 \mu\text{m}$. For visual clarity, cross-hairs are added.

4.4 Data Processing

The data evaluation to determine the shifts of the SPP resonance at different voltages is performed with a home-built Python program which automatizes the evaluation of a specific measurement cycle.

Fig. 4.6 shows the user interface of the software which was developed with the PyQt4 library [42]. In general, the software is programmed such that it can be used for the evaluation of plasmonic resonant shifts upon applied voltages (as shown in Fig. 4.6) or to evaluate batches of simple reflection measurements (will not be explained further). The first evaluation step is to define whether or not the reference data has to be normalized by the reflectivity of silicon or silver. Then, the measured data comprising of the sample's reflection data ('Load Raw Data'-button), the background signal and reference data can be loaded with the 'Data Load Buttons'. The software will automatically load the log file which is associated with the measurement and show parameters such as minimum and maximum voltage, number of spectra or delay time in the Parameter Overview. These parameters will be used in the further evaluation to label the generated plots. The 'make Spectrum Plot'-button and the 'make Ref Data Plot'-button can be used to plot the unprocessed raw data. The result viewer allows to examine evaluated plots which can be selected from the 'result overview' tabs.

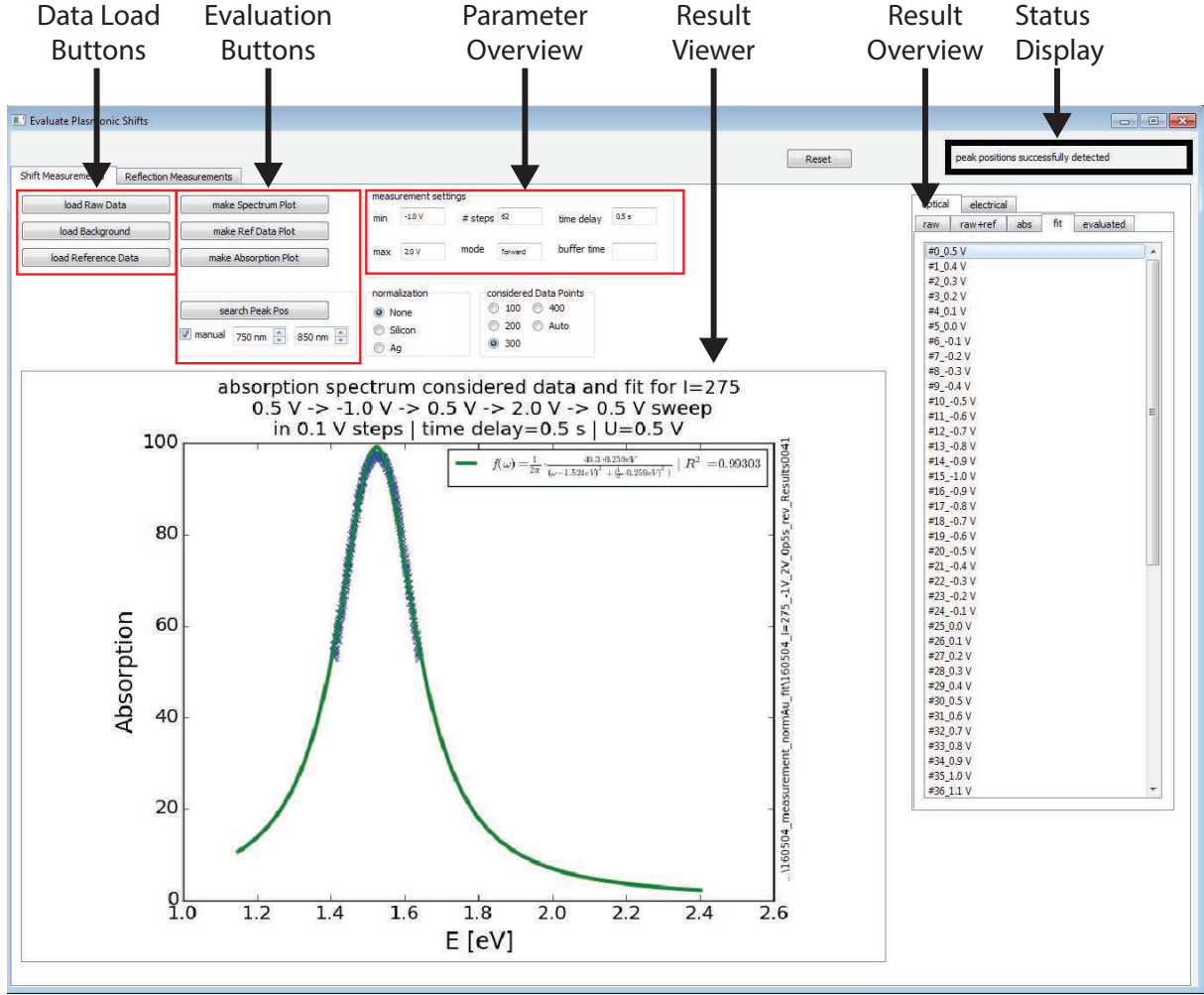


Fig. 4.6: User interface of the Python programme which is used for data analysis.

The actual evaluation of data starts with calculating the absorption spectra and generating absorption plots. The absorption spectrum $\text{Abs}_{\text{HA}}(\lambda)$ of a hole array is determined by considering the reflected signal $I_{\text{HA}}(\lambda)$ (Fig. 4.7a, blue line) on the hole array and a reference signal $I_{\text{ref}}(\lambda)$ either from the pristine gold film next to the hole array or from a silicon sample (Fig. 4.7a, green line) as well as the background spectrum $I_{\text{bg}}(\lambda)$ of the spectrometer. The absorption is then calculated according to

$$\text{Abs}_{\text{HA}}(\lambda) = \frac{I_{\text{HA}}(\lambda) - I_{\text{bg}}(\lambda)}{I_{\text{ref}}(\lambda) - I_{\text{bg}}(\lambda)} \quad (4.1)$$

An exemplary absorption spectrum of a hole array is shown in Fig. 4.7b for normalization with the unperforated gold film. The distinct peak at about 810 nm can be attributed to the SPP resonance whereas the peak at around 650 nm can be explained with a small mismatch in the fabry resonance absorption in the pristine and perforated gold film and the noisy signal at the margins are due to low signal-to-noise ratios.

In a further step, the absorption spectrum is converted from wavelength to energy space and a Lorentzian function (Eq. 4.2) is least-square fitted to the peak in order to detect

parameters such as peak position, relative peak height and peak width (Fig. 4.7c). Here, Γ denotes the peak width, E_0 the peak position and A is the amplitude parameter. The number of considered data points can be selected in the software. For an optimal fit, the software makes sure that the data points are equally distributed around the peak (see Fig. 4.7c, blue crosses) before it performs the fit. In case that there are data points which exceed the amplitude of the SPP resonance, it is possible to restrict the fit range with the spin boxes under the 'search Peak Pos'-button.

$$L(E) = \frac{A}{\pi} \frac{\frac{1}{2}\Gamma}{(E - E_0)^2 + (\frac{1}{2}\Gamma)^2} \quad (4.2)$$

This procedure is performed for all spectra of a dataset so that the peak parameters can be extracted as a function of applied voltage. Fig. 4.7 displays exemplary plots of peak position (d), peak width (e) and maximum absorption (f) as a function of voltage.

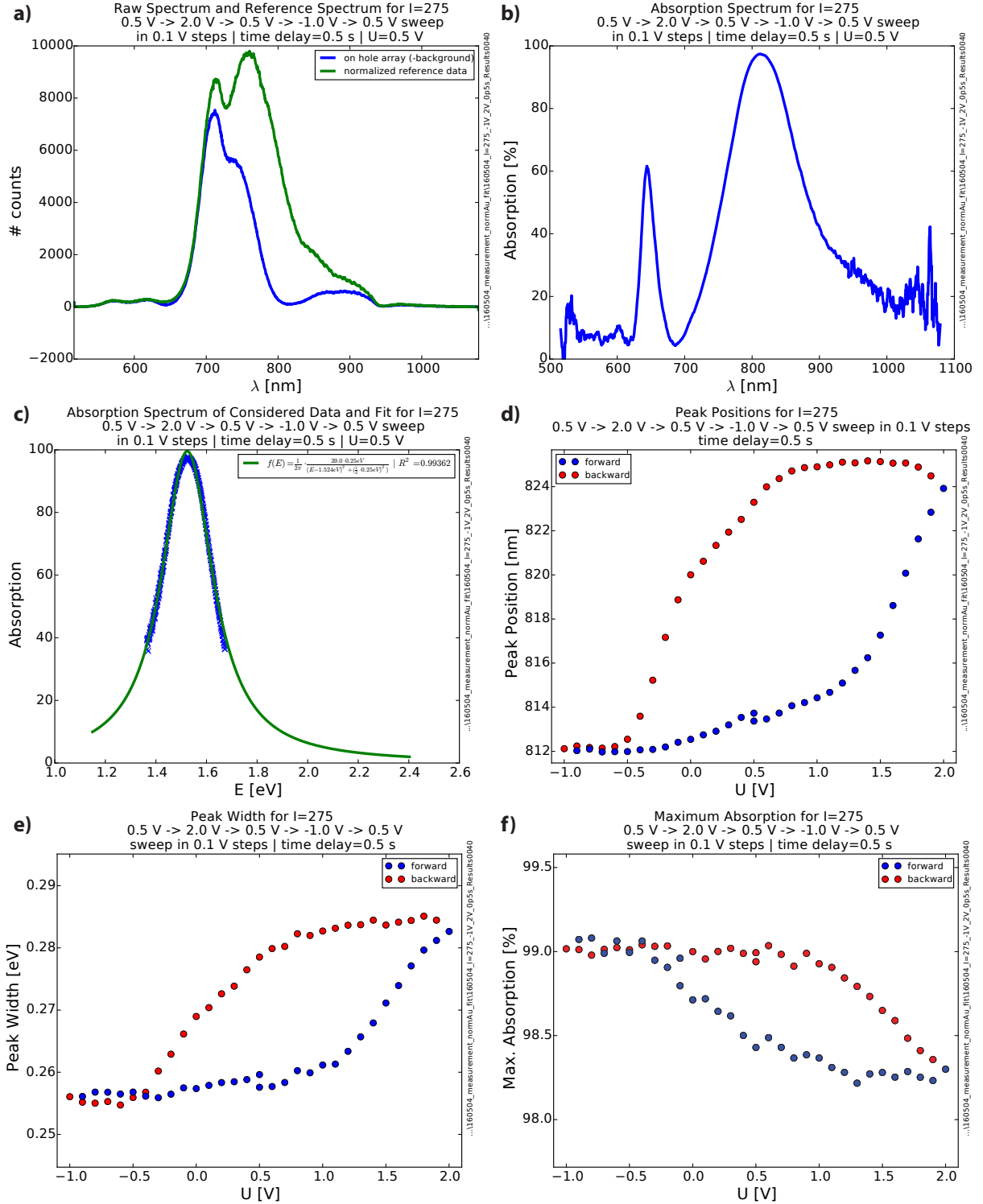


Fig. 4.7: a) Exemplary raw spectra on hole array and pristine gold film, both corrected for the background, b) relative absorption spectrum of the hole array, calculated according to eq. (4.1) and smoothed with Savitzky-Golay filter, c) Lorentzian fit (green line) to absorption spectrum in energy space (blue crosses). The inset displays the obtained fit parameters of the Lorentzian function d)-e) Exemplary plots of readily evaluated data: d) Peak Position vs. Applied Voltage, e) Peak Width vs. Applied Voltage, f) Maximum Absorption vs. Applied Voltage

Chapter 5

Supplementary Information

5.1 Dependence of SPP Resonance on Gold Thickness

The dependence of characteristic SPP parameters on the thickness of the gold film is modeled with FDTD simulations. Fig. S1 shows the peak position (a), peak width (b) and peak amplitude (c) as a function of hole diameter for gold thicknesses of 20, 22 and 24 nm. The peak position is very sensitive to the thickness of the gold film and changes by about 15 nm for a thickness difference of 2 nm. In contrast to this, the thickness dependence is weaker for peak width and amplitude.

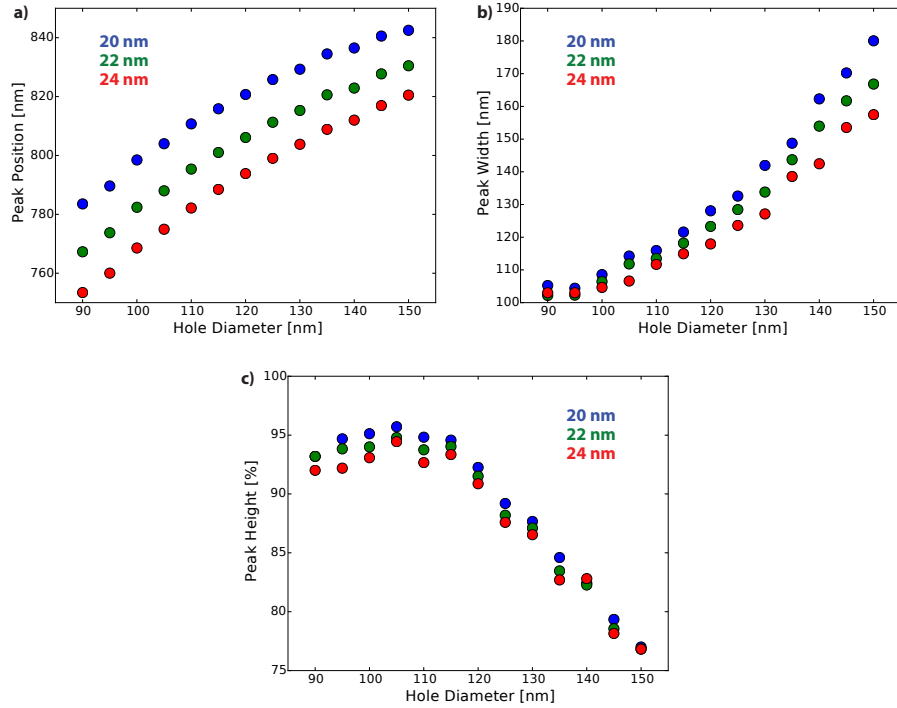


Fig. S1: Simulated influence of differently thick gold layers on a) peak position, b) peak width and c) peak amplitude.

5.2 Brendel-Bormann Model

Table S1 lists the Brendel-Bormann parameters of gold as determined by Rakic et al. [7].

j	f_j	Γ_j [eV]	ω_j [eV]	σ_j
0	0.770	0.050	-	-
1	0.054	0.074	0.218	0.742
2	0.050	0.035	2.885	0.349
3	0.312	0.083	4.069	0.830
4	0.719	0.125	6.137	1.246
5	1.648	0.179	27.970	1.795

$$\omega_p = 9.03 \text{ eV}$$

Table S1: Brendel-Bormann parameters for gold as found by Rakic et al. [7]

5.3 Calculated Relative Changes in Charge Density and Refractive Index

This chapter comprises of a tabular overview of the calculated changes in relative charge density and refractive index. These values are the basis for the FDTD simulations whose results are displayed and discussed in chapter 3.4.1-3.4.3.

5.3.1 Electric Double Layer Capacitance

Table S2 contains the calculated relative change in charge density for the case of an electrostatic double layer. The layer thicknesses for which this is calculated are 0.5 and 5 nm.

U [V]	C [$\mu\text{F}/\text{cm}^2$]	Q [C/m ²]	n_{area} [$\times 10^{18} \text{ m}^{-2}$]	$n_{5\text{nm}}$ [$\times 10^{27}$]	n'/n_0	$n_{0.5\text{nm}}$ [$\times 10^{27}$]	n'/n_0
0.00	0.00	0.00	0.000	0.00	1.000	0.000	1.000
0.25	6.25	0.02	0.098	0.020	1.000	0.195	0.997
0.50	12.50	0.06	0.390	0.078	0.999	0.78	0.987
0.75	18.75	0.14	0.878	0.176	0.997	1.76	0.970
1.00	25.00	0.25	1.560	0.312	0.995	3.12	0.947
1.25	31.25	0.39	2.440	0.488	0.992	4.88	0.917
1.50	37.50	0.56	3.510	0.702	0.988	7.02	0.881
1.75	43.75	0.77	4.780	0.956	0.984	9.56	0.838
2.00	50.00	1.00	6.240	1.250	0.979	12.50	0.788

Table S2: Relative change in charge density n'/n_0 derived from measured AC capacitance and calculated for a 5 nm and 0.5 nm thick layer of altered charge density. U is the applied voltage, C the measured (and extrapolated) AC capacitance, Q is the charge density which calculates $Q = C \cdot U$ and n_{area} is the aerial number density of electrons. $n_{5\text{nm}}$ and $n_{0.5\text{nm}}$ are the total number of electrons in a 5 and 0.5 nm thick layer, respectively.

Table S3 lists the calculated refractive index in an 8 nm thick electric double layer constituted by TFSI molecules.

U [V]	C [$\mu\text{F}/\text{cm}^2$]	n_{TFSI} [10^{27}m^{-3}]	$n_{\text{H}_2\text{O}}$ [10^{27}m^{-3}]	refractive index
0.00	0.00	0.000	33.30	1.3170
0.25	6.25	0.012	33.20	1.3171
0.50	12.50	0.049	32.91	1.3177
0.75	18.75	0.110	32.42	1.3186
1.00	25.00	0.195	31.73	1.3197
1.25	31.25	0.305	30.85	1.3212
1.50	37.50	0.439	29.77	1.3231
1.75	43.75	0.597	28.50	1.3252
2.00	50.00	0.780	27.03	1.3278

Table S3: Calculated number densities of TFSI and H_2O and refractive indices for a 8 nm thick EDL. U is the applied voltage, C the measured (and extrapolated) AC capacitance. The number densities are calculated with Eq. 3.3 and 3.4, respectively. The refractive index is calculated from Eq. 2.11.

5.3.2 Capacitance Due to Chemisorption

Table S4 shows the calculated relative change in charge density for a 0.5 and 5 nm thick layer for measured DC capacitances. Note that our model predicts more than complete depletion of free charge carriers in the case of a 0.5 nm thick layer.

U [V]	C [$\mu\text{F}/\text{cm}^2$]	Q [C/m^2]	n_{area} [$\times 10^{18}\text{m}^{-2}$]	$n_{5\text{nm}}$ [$\times 10^{27}$]	n'/n_0	$n_{0.5\text{nm}}$ [$\times 10^{27}$]	n'/n_0
0.00	207	0.00	0.00	0.00	1.000	0.00	1.000
0.25	235	0.59	3.67	0.73	0.988	7.33	0.876
0.50	193	0.97	6.02	1.20	0.980	12.05	0.796
0.75	175	1.31	8.19	1.64	0.972	16.38	0.722
1.00	223	2.23	13.92	2.78	0.953	27.84	0.528
1.25	303	3.79	23.64	4.73	0.920	47.28	0.199
1.50	408	6.12	38.20	7.64	0.871	76.40	-0.295
1.75	429	7.51	46.86	9.37	0.841	93.72	-0.588
2.00	104	2.08	12.98	2.60	0.956	25.96	0.560

Table S4: Relative change in charge density n'/n_0 derived from measured AC capacitance and calculated for a 5 nm and 0.5 nm thick layer of altered charge density. U is the applied voltage, C the measured DC capacitance, Q is the charge density which calculates $Q = C \cdot U$ and n_{area} is the aerial number density of electrons. $n_{5\text{nm}}$ and $n_{0.5\text{nm}}$ are the total number of electrons in a 5 and 0.5 nm thick layer, respectively.

Table S5 shows the calculated altered refractive index in the ionic liquid for measured DC capacitances.

U [V]	C [$\mu\text{F}/\text{cm}^2$]	n_{TFSI} [10^{27}m^{-3}]	$n_{\text{H}_2\text{O}}$ [10^{27}m^{-3}]	refractive index
0.00	207.00	0.000	33.30	1.3170
0.25	235.00	0.229	31.46	1.3202
0.50	193.00	0.376	30.27	1.3221
0.75	175.00	0.512	29.19	1.3241
1.00	223.00	0.870	26.31	1.3291
1.25	303.00	1.477	21.43	1.3375
1.50	408.00	2.387	14.12	1.3504
1.75	429.00	2.929	9.77	1.3581
2.00	104.00	0.811	26.78	1.3282

Table S5: Calculated number densities of TFSI and H₂O and refractive indices for a 16 nm thick layer of chemisorbed ions. U is the applied voltage, C the measured DC capacitance. The number densities are calculated with Eq. 3.3 and 3.4, respectively. The refractive index is calculated from Eq. 2.11.

Chapter 6

References

- [1] B. Sharma, R. R. Frontiera, A.-I. Henry, E. Ringe, and R. P. Van Duyne, “SERS: Materials, applications, and the future,” *Mater. Today*, vol. 15, no. 1-2, pp. 16–25, 2012.
- [2] I. Ament, J. Prasad, A. Henkel, S. Schmachtel, and C. Sönnichsen, “Single unlabeled protein detection on individual plasmonic nanoparticles,” *Nano Lett.*, vol. 12, no. 2, pp. 1092–1095, 2012.
- [3] H. A. Atwater and A. Polman, “Plasmonics for improved photovoltaic devices.,” *Nat. Mater.*, vol. 9, no. 3, pp. 205–213, 2010.
- [4] S. C. Warren, D. A. Walker, and B. A. Grzybowski, “Plasmoelectronics: Coupling plasmonic excitation with electron flow,” *Langmuir*, vol. 28, no. 24, pp. 9093–9102, 2012.
- [5] M. T. Sheldon, J. V. D. Groep, A. M. Brown, H. A. Atwater, and A. Polman, “Plasmo-electric potentials in metal nanostructures,” *Science*, vol. 346, no. 6211, pp. 828–831, 2014.
- [6] U. Kreibig and M. Vollmer, *Optical Properties of Metal Clusters*. Springer, 1995.
- [7] A. D. Rakic, A. B. Djuricic, J. M. Elazar, and M. L. Majewski, “Optical properties of metallic films for vertical-cavity optoelectronic devices.,” *Appl. Opt.*, vol. 37, no. 22, pp. 5271–5283, 1998.
- [8] R. Brendel and D. Bormann, “An infrared dielectric function model for amorphous solids,” *J. Appl. Phys.*, vol. 71, no. 1, pp. 1–7, 1992.
- [9] M. Thèye, “Investigation of the Optical Properties of Au by Means of thin Semitransparent Films,” *Phys. Rev. B*, vol. 2, no. 8, pp. 3060–3078, 1971.
- [10] S. A. Maier, *Plasmonics: Fundamentals and Applications*. Springer, 2004.
- [11] L. Novotny and B. Hecht, *Principles of Nano-Optics*. Cambridge University Press, 2006.

-
- [12] W. L. Barnes, A. Dereux, and T. W. Ebbesen, "Surface plasmon subwavelength optics.," *Nature*, vol. 424, pp. 824–830, 2003.
 - [13] D. Rosenblatt, A. Sharon, and A. A. Friesem, "Resonant grating waveguide structures," *IEEE J. Quantum Electron.*, vol. 33, no. 11, pp. 2038–2059, 1997.
 - [14] K. E. Oughstun and N. A. Cartwright, "On the Lorentz-Lorenz formula and the Lorentz model of dielectric dispersion," *Opt. Express*, vol. 11, no. 13, pp. 1541–1546, 2003.
 - [15] Y. K. Kang and M. S. Jhon, "Additivity of Atomic Static Polarizabilities and Dispersion Coefficients," *Theor. Chim. Acta*, vol. 61, pp. 41–48, 1982.
 - [16] S. Link and M. A. El-Sayed, "Shape and size dependence of radiative, non-radiative and photothermal properties of gold nanocrystals," *Int. Rev. Phys. Chem.*, vol. 19, no. 3, pp. 409–453, 2000.
 - [17] A. M. Brown, M. T. Sheldon, and H. A. Atwater, "Electrochemical Tuning of the Dielectric Function of Au Nanoparticles," *ACS Photonics*, vol. 2, no. 4, pp. 459–464, 2015.
 - [18] R. Chapman and P. Mulvaney, "Electro-optical shifts in silver nanoparticle films," *Chem. Phys. Lett.*, vol. 349, no. 5-6, pp. 358–362, 2001.
 - [19] C. Novo, A. M. Funston, A. K. Gooding, and P. Mulvaney, "Electrochemical charging of single gold nanorods," *J. Am. Chem. Soc.*, vol. 131, no. 41, pp. 14664–14666, 2009.
 - [20] S. K. Dondapati, M. Ludemann, R. Müller, S. Schwieger, A. Schwemer, B. Händel, D. Kwiatkowski, M. Djiango, E. Runge, and T. A. Klar, "Voltage-induced adsorbate damping of single gold nanorod plasmons in aqueous solution," *Nano Lett.*, vol. 12, no. 3, pp. 1247–1252, 2012.
 - [21] A. Dahlin, R. Zahn, and J. Vörös, "Nanoplasmonic sensing of metalhalide complex formation and the electric double layer capacitor," *Nanoscale*, vol. 4, pp. 2339–2351, 2012.
 - [22] K. L. Kelly, E. Coronado, L. L. Zhao, and G. C. Schatz, "The Optical Properties of Metal Nanoparticles: The Influence of Size, Shape, and Dielectric Environment," *J. Phys. Chem. B*, vol. 107, pp. 668–677, 2003.
 - [23] Y. Kim, R. C. Johnson, and J. T. Hupp, "Gold Nanoparticle-Based Sensing of Spectroscopically Silent Heavy Metal Ions," *Nano Lett.*, vol. 1, no. 4, pp. 165–167, 2001.
 - [24] J. R. Piper and S. Fan, "Total Absorption in a Graphene Monolayer in the Optical Regime by Critical Coupling with a Photonic Crystal Guided Resonance," *ACS Photonics*, vol. 1, pp. 347–353, 2014.
 - [25] "Lumerical Solutions, Inc. <http://www.lumerical.com/tcad-products/fdtd/>."
-

-
- [26] J. Braun, B. Gompf, G. Kobiela, and M. Dressel, “How holes can obscure the view: Suppressed transmission through an ultrathin metal film by a subwavelength hole array,” *Phys. Rev. Lett.*, vol. 103, no. 20, pp. 1–4, 2009.
 - [27] T. Rindzevicius, Y. Alaverdyan, B. Sepulveda, T. Pakizeh, M. Käll, R. Hillenbrand, J. Aizpurua, and F. J. García de Abajo, “Nanohole plasmons in optically thin gold films,” *J. Phys. Chem. C*, vol. 111, no. 3, pp. 1207–1212, 2007.
 - [28] H. Yuan, H. Shimotani, J. Ye, and S. Yoon, “Electrostatic and Electrochemical Nature of Liquid-Gated Electric-Double-Layer Transistors Based on Oxide,” *J. Am. Chem. Soc.*, vol. 132, no. 13, pp. 18402–18407, 2010.
 - [29] T. Fujimoto and K. Awaga, “Electric-double-layer field-effect transistors with ionic liquids,” *Phys. Chem. Chem. Phys.*, no. 15, pp. 8983–9006, 2013.
 - [30] C. P. Byers, B. S. Hoener, W.-S. Chang, M. Yorulmaz, S. Link, and C. F. Landes, “Single-Particle Spectroscopy Reveals Heterogeneity in Electrochemical Tuning of the Localized Surface Plasmon,” *J. Phys. Chem. B*, vol. 118, pp. 14047–14055, 2014.
 - [31] W. Mönch, *Semiconductor Surfaces and Interfaces*. Springer, 2001.
 - [32] H. Lüth, *Solid Surfaces, Interfaces and Thin Films*. Springer, 2010.
 - [33] A. J. Bard, L. R. Faulkner, E. Swain, and C. Robey, *Electrochemical Methods - Fundamentals and Applications*. Wiley, 2000.
 - [34] K. J. Miller, “Additivity Methods in Molecular Polarizability,” *J. Am. Chem. Soc.*, vol. 112, pp. 8533–8542, 1990.
 - [35] Chemicalize.org — Water Molecule, “www.chemicalize.org/structure/#!mol=water, date accessed: 07-06-2016.”
 - [36] Chemicalize.org — TFSI molecule, “<http://www.chemicalize.org/structure/#!mol=bistriflyimide+anion>, date accessed: 07-06-2016.”
 - [37] M. Bauer and M. Aeschlimann, “Dynamics of excited electrons in metals, thin films and nanostructures,” *J. Electron Spectros. Relat. Phenomena*, vol. 124, pp. 225–243, 2002.
 - [38] B. N. J. Persson, “Polarizability of small spherical metal particles: influence of the matrix environment,” *Surf. Sci.*, vol. 281, no. 1-2, pp. 153–162, 1993.
 - [39] M. Kettner, I. Vladimirov, A. J. Strudwick, M. G. Schwab, R. T. Weitz, M. Kettner, I. Vladimirov, A. J. Strudwick, and G. Schwab, “Ionic gel as gate dielectric for the easy characterization of graphene and polymer field-effect transistors and electrochemical resistance modification of graphene,” *J. Appl. Phys.*, vol. 118, p. 025501, 2015.
 - [40] J. S. Schildkraut, “Long-range surface plasmon electrooptic modulator,” *Appl. Opt.*, vol. 27, no. 21, pp. 4587–4590, 1988.
-

-
- [41] M. Luennemann, U. Hartwig, G. Panotopoulos, and K. Buse, “Electrooptic properties of lithium niobate crystals for extremely high external electric fields,” *Appl. Phys. B Lasers Opt.*, vol. 76, no. 4, pp. 403–406, 2003.
- [42] “PyQt Python Library — <https://wiki.python.org/moin/PyQt>.”

